



Repositorio Institucional de la Universidad Autónoma de Madrid

<https://repositorio.uam.es>

Esta es la **versión de autor** del artículo publicado en:
This is an **author produced version** of a paper published in:

Advanced Materials 30.2 (2018): 1703771

DOI: <https://doi.org/10.1002/adma.201703771>

Copyright: © 2017 Wiley - VCH Verlag GmbH & Co. KGaA, Weinheim

El acceso a la versión del editor puede requerir la suscripción del recurso

Access to the published version may require subscription

DOI: 10.1002/ ((please add manuscript number))

Article type: Progress Report

Recent progress on antimonene: a new bidimensional material

By Pablo Ares, Juan José Palacios, Gonzalo Abellán, Julio Gómez-Herrero and Félix Zamora**

Dr. P.A., Dr. J.J.P., Prof. J.G.H.
Departamento de Física de la Materia Condensada
Universidad Autónoma de Madrid, Madrid E-28049 (Spain)
E-mail: julio.gomez@uam.es

Dr. F. Z.
Departamento de Química Inorgánica
Universidad Autónoma de Madrid, Madrid E-28049 (Spain)
E-mail: felix.zamora@uam.es

Dr. J.J.P., Prof. J. G. H., Dr. F. Z.
Condensed Matter Physics Center (IFIMAC)
Universidad Autónoma de Madrid, Madrid E-28049 (Spain)

Dr. G.A.
Department of Chemistry and Pharmacy and Joint Institute of Advanced Materials and Processes (ZMP)
Friedrich-Alexander-Universität Erlangen-Nürnberg (FAU), Henkestrasse 42, 91054 Erlangen and Dr.-Mack Strasse 81, 90762 Fürth, (Germany)

Dr. F. Z.
Instituto Madrileño de Estudios Avanzados en Nanociencia (IMDEA-Nanociencia)
Cantoblanco, Madrid E-28049 (Spain)

Dr. F. Z.
Institute for Advanced Research in Chemical Sciences (IAdChem)
Universidad Autónoma de Madrid, Madrid E-28049 (Spain)

Keywords: 2D Materials, Antimonene, Black Phosphorus, Theoretical Calculations, 2D Materials Preparation

Antimonene, defined in *sensu stricto* as a single layer of antimony atoms, has recently been the focus of numerous theoretical works predicting a variety of interesting properties and is quickly attracting the attention of the scientific community. However, what places antimonene on a different category from other two-dimensional crystals is its strong spin-orbit coupling

and a drastic evolution of its properties from the monolayer to the few-layer system. The recent isolation of this novel two-dimensional material pushes even further the interest for antimonene. Here, a review of both theoretical predictions and experimental results is compiled. We begin by giving an account of the calculations anticipating an electronic band structure suitable for optoelectronics and thermoelectric applications in monolayer form and a topological semimetal in few-layer form. Second, the different approaches to produce antimonene –mechanical and liquid phase exfoliation, and epitaxial growth methods– are reviewed. In addition, this work also reports the main characterization techniques used to study this exotic material. This review provides insights for further exploring the appealing properties of antimonene and puts forward the opportunities and challenges for future applications from (opto)electronic devices fabrication to biomedicine.

1. Introduction

Graphene, a single layer of graphite, was isolated in 2004 by Geim and Novoselov^[1]. Before this date, two-dimensional (2D) crystals belonged in the realm of academic curiosities. The rising of graphene research demonstrates both its fundamental scientific interest and its potential applications on many different technological fields including electronics, gas storage or separation, high performance sensors, catalysis, membranes or hard coatings, just to name a few. This extraordinary scientific success^[2] opened the door to new families of 2D materials born with the aim of complementing the list of graphene physical properties.^[3] For example, as is well-known, graphene is a semimetal with no band gap, preventing its use for many practical electronic and optoelectronic applications.

Currently, the field of 2D materials is among the most active research areas in materials science and nanoscience.^[3-4] In the search of novel 2D materials transition metal dichalcogenides have largely dominated the research spectrum because most of them present a band gap in the range of 1.5–2.5 eV,^[5] which can be tuned by controlling the number of

layers, stress level and chemical functionalization. However, this range of band gaps makes them not very appropriate for optoelectronics devices where lower values in the 0.1–1 eV range are usually demanded.^[6] Very recently, scientists have also been able to isolate and characterize phosphorene, a 2D allotrope of black phosphorus (BP).^[7] The direct band gap of single-layer phosphorene is about 1.5 eV,^[6] and thereof interesting for electronics and ultra-fast optoelectronics. Phosphorene has been intensively studied over the past two years; however, it suffers from a remarkable reactivity under environmental conditions. Indeed, exfoliated flakes of phosphorene are very oxophilic, what makes the BP surface hydrophilic, uptaking moisture from air and forming phosphoric acid and related species, finally degrading the material.^[8] The degradation of BP flakes can be clearly observed by measuring their topography over hour periods and by characterizing their electrical transport properties as a function of time.^[9] Therefore, the discovery and production of novel 2D materials exhibiting appropriate band gaps and stability in atmospheric conditions is still a challenge of the greatest importance for technology.

Phosphorus can be found in group 15 in the periodic table of elements. Antimony belongs to the same group of elements, also called pnictogens, showing silvery lustrous, non-hygroscopic, gray semimetal features. Its layered structure, somehow, resembles the one of BP, but with shorter out-of-plane atom-to-atom distances, therefore indicative of stronger interlayer interactions, hampering mechanical exfoliation. While the properties of single and few layers of antimony had been previously explored from a theoretical viewpoint, isolation and characterization in the laboratory is a much more recent scientific advance. In this review article, we summarize the state-of-the-art of current research in antimonene, a single layer of antimony, both from a theoretical perspective and from the progress made on the preparation, including: mechanical exfoliation, liquid phase exfoliation and epitaxial growth methods. For each preparation method we describe in some detail the techniques used to characterize this novel material in the laboratory.

Disregarding nomenclature issues, from a fundamental point of view, antimonene is unique among other 2D materials because of its strong spin-orbit coupling. 2D topological material^[10] and their large spectrum of potential applications originate in a strong atomic spin-orbit coupling. Monolayer antimonene is, in this sense, a trivial semiconductor, but can be tuned into a 2D topological insulator by strain. However, and in our opinion of even more potential interest, is the fact that few-layer antimonene (starting at approx. 7-8 layers) is a 3D topological *semimetal*. Despite presenting bulk carriers, it also features topologically protected surface states, as more standard topological insulators. The possibilities of this surface states from an electronic and, possibly also, chemical points of view are only beginning to be explored and understood. The completely new properties that emerge when transitioning from the monolayer to the few-layer system makes antimonene one of a kind in the 2D crystal catalogue and thus, we can hardly imagine what this will bring about in terms of applications.

Finally, as it has been demonstrated in several experimental works, the high stability of antimonene under ambient conditions and, particularly, in water together with its physical properties, open new attractive applications for this novel material.

For the sake of clarity, we should mention that, since there are no double bonds in the antimony lattice structure, as is the case of graphite, the name antimonene is not completely correct. However, we will use it as far as it is the most accepted nomenclature in the literature.

2. Theoretical work

The knowledge on antimonene is currently unbalance: the amount of theoretical work on antimonene largely exceeds its experimental counterpart. Density functional theory (DFT) has allowed researchers to make a number of quantitative predictions of the electronic and structural properties of antimonene. Two types of theoretical work, quite clearly separated in time (and in researcher communities), can be found in the literature. The most recent

publications refer to monolayer antimonene (or occasionally bilayer antimonene) and can be found in the context of new 2D crystals. The second one, which goes a few years back in time, refers to few-layer (FL) antimonene (or Sb thin films), and can be found in the context of 3D topological insulators.^[10] The physical properties of antimonene change quite drastically from the monolayer to FL systems (these generally considered to be in the range of 10 – 100 layers) and both deserve a separate discussion. Here we mostly focus on the monolayer case, but also present, at the end of this section, a brief account of the research on FL antimonene.

2.1. Monolayer antimonene

2.1.1. Band structure

Although the band structure of monolayer antimonene had been reported before in a different context (see Reference ^[11] and discussion in next section), the raise in the interest for this material as a promising 2D semiconductor started with the theoretical work of Zhang *et al.*^[12] The authors reported DFT calculations of the band structure of monolayer antimonene (in its hexagonal β form) featuring an indirect gap of 2.28 eV (**Figure 1**) and stressed the fact that this material could potentially be useful for optoelectronic applications in the ultraviolet (UV) regime. Around the same time a similar study was reported showing also an indirect gap, but of smaller value (0.76 eV).^[13] The difference can be attributed to the different nature of the functionals used, giving hybrid functionals larger gap values and therefore these being more reliable. An intermediate (also indirect) gap value of 1.55 eV was reported shortly afterwards following the steps of Reference ^[12a], but now taking into account spin-orbit coupling (SOC), which, as shown below, happens to play a non-trivial role.^[14] A number of similar calculations have been reported more recently, giving a fairly wide range of gap values depending on the DFT implementation used and whether SOC is considered or not, but the indirect nature of the gap is a common feature to all of them.^[13, 15] To the best of our knowledge, so far, there is not an experimental determination of this figure that could help to

discriminate between the different theoretical predictions. Hence, there is clear open challenge for measurements to shed light on the large scatter in the size of antimonene theoretical band gap.

2.1.2. Allotropes and structural stability

The most commonly studied antimonene structure (β -antimonene) is not the only possible one. DFT calculations have been performed for other allotropic forms (**Figure 2**), including the α , γ , and δ phases.^[13] The results have shown that, other than the β structure, the only stable one is the α allotrope. The crystallographic structure of this phase corresponds to a rectangular Bravais lattice with four atoms in the unit cell. Similar in many aspects to a black phosphorus monolayer or phosphorene,^[16] α -antimonene presents two atomic sublayers, where the two unit cell atoms that belong to the same sublayer are not exactly located in the same plane (Figure 2). The relative stability of α - and β -antimonene has been studied by comparing the cohesive energy of the different allotropic forms. The α form presents, in general, a larger cohesive energy than β form when using LDA (≈ 60 meV) and van-der-Waals corrected DFT-D2 (≈ 30 meV), although both phases become almost degenerate when the more standard GGA(PBE) is used instead.^[13, 15g] Also the phonon free energy has been computed finding that the difference between both phases in the range of temperatures 0-600 K was less than 15 meV/atom. This suggests that both phases are comparable in their structural stability and, in principle, both could be found in experiments. In contrast to β -antimonene, the band gap of α -antimonene is direct and, in addition, its value is much smaller (≈ 0.2 eV) than that of the β counterpart.^[15g] Otherwise stated, antimonene must be understood as β -antimonene throughout this review.

2.1.3. Optical response

DFT band structure calculations, even when correctly reproducing the magnitude and nature of the gap, only give a superficial idea of what to expect for the optical properties of materials. Predictions for the use of antimonene as a material for optical applications may only arise from the calculation of its dielectric function. The most common approach in the literature to the calculation of this is based on the random phase approximation (RPA). The complex dielectric function and concomitant refractive index, absorption coefficients, electron loss spectra (EELS), or optical reflectivity, for example, have been reported in the energy range between 0 and 21 eV.^[15d] The absorption process is expected to start in the infrared part of the spectrum, but presents a maximum in the UV region. The values of the refractive index are 2.3 (α -antimonene) and 1.5 (β -antimonene) at zero frequency and scale up to 3.6 and 2.0 for α -antimonene and β -antimonene, respectively, in the UV region. The dielectric function as long as the EELS results feature plasmon energies near 9 eV, indicating that in this part of the spectrum antimonene behaves like a metal as far as the reflection of light is concerned. Actually, reflection rises there up to 86% for α -antimonene. Interestingly, for β -Sb, when the polarization direction of the incident light is out of plane, the reflectivity in the visible region is high and the absorption is almost negligible, indicating that β -Sb is a polarizationally transparent material.^[15g] These calculations show that antimonene may be potentially useful for optoelectronic devices or solar cell applications and, in general for novel devices combining light emission, modulation, and detection functions.

2.1.4. Adsorbates

Gas sensing, in particular directed towards polluted or toxic gas, is a very important research field with practical ramifications in studies related to environmental pollution, medical diagnosis, industrial quality control, or agricultural production. Recent work predicted that molecules such as H₂, N₂, O₂, CO, and H₂O do not form strong chemical bonds with

antimonene and do not dissociate on it either. These molecules are weakly physisorbed with a small binding energy, which does not affect the fundamental properties of the host.^[17]

Experimental evidence also corroborates the negligible adsorption of water on antimonene.^[18]

Molecules present in polluted gases such as NH_3 , SO_2 , or NO also physisorb on the surface, although these present stronger adsorption energies. This has been attributed to the frontier orbitals of the molecules, which are closer to the Fermi level and therefore more prone to hybridizations. The small or moderate values of the adsorption energies, along with the physical nature of the adsorption process, indicate that antimonene is potentially useful as a sensor for polluted gases. Interestingly, the adsorption of NO_2 on antimonene is an activated process with a stronger chemisorption character, suggesting that antimonene can be used as a disposable sensor or metal-free catalyst for detection or catalysis of this molecule.^[17b]

Adatoms, such as H, Li, C, B, O, N, Al, In, Si, P, Cl, Ti, As, and Sb have been found to chemisorb with significant binding energy, locally modifying the atomic and electronic structures (**Figure 3**).^[17a] Boron and C adatoms can be embedded into β -antimonene leading to a local reconstruction of the crystal. Nitrogen, for example, gives rise to Stone-Wales type defects. Localized states, originated from the presence of different adatoms give rise to a diversity of effects in the band structure. For instance, the lowest conduction and highest valence bands of α -antimonene present an accused curvature, which combined with adatom states, present a variety of new features. In addition, specific adatoms can lead to the creation of magnetic moments and spin polarization conferring a half-metallic character to antimonene.

2.1.5. Nanoribbons

Nanoribbons “cut out of” a 2D crystal can offer additional electronic features to those present in the 2D bulk form. These new features will mainly come from quantum confinement effects and the possible existence of edge states. The properties (and even the very existence) of these usually depend on the crystallographic orientation of the edge. Again through DFT

calculations, the electronic and transport properties of antimonene nanoribbons have been studied.^[19] It was found, maybe not surprisingly given the extensive existing literature on graphene nanoribbons,^[20] that their electronic band structure depends on the shape of the edge (**Figure 4**). All armchair antimonene nanoribbons (β -phase) maintain, same as in bulk, an indirect band gap, while the *zig-zag* ones change into direct-gap semiconductors. As expected, the gap increases with quantum confinement and, for both armchair and *zig-zag* nanoribbons, scales inversely proportional to the width (see panels d, e, and f in **Figure 5**). Quantum confinement appears, however, to be stronger in the armchair nanoribbons than in the *zig-zag* ones, producing larger band gaps in the former case. Compared to phosphorene, and due to rather characteristic charge distributions near the band edges, their large deformation potential constants translate into small carrier mobilities in the range of 10^1 - 10^2 cm²/Vs. This study shows that antimonene nanostructures possess alternative electronic properties with potential novel applications in nanoelectronics.

Again inspired by graphene literature,^[20] it was somewhat expected that spin-related instabilities could appear on the edges of nanoribbons. This has been investigated in Reference ^[21]. In this work, based on DFT calculations, the authors reported the existence of edge magnetism in *zig-zag* puckered V-ene (phosphorene, arsenene, and antimonene) nanoribbons (ZVNRs). A strong Peierls instability could be anticipated due to the existence of half-filled bands with a Fermi level crossing at the midpoint in the Brillouin zone. This instability could be removed by two different mechanisms: firstly, a spin density wave (SDW) originating in electron-electron interactions and, secondly, a charge density wave (CDW) aided by electron-phonon coupling. An antiferromagnetic Mott-insulating state associated with the SDW was found to be the ground state of ZVNRs. In addition, the SDW features several unexpected characteristics: 1) when compared to other nanoribbon systems, the magnetic moments are aligned antiparallel on each *zig-zag* edge and their magnitude is almost independent on the width of these; 2) when compared with other systems that exhibit a SDW,

the magnetic moments and associated band gap are unexpectedly large, pointing towards a higher SDW transition temperature; 3) finally, the SDW was shown to be amenable to modifications by strain or charge doping, which certainly adds interest from the application viewpoint.

2.1.6. Antimonene-based heterostructures

The experimental isolation and basic characterization of antimonene^[18] was preceded by similar reports for phosphorene^[16] and bismuthene.^[22] Despite arsenene being absent from this list of group 15 2D elemental materials, its structural stability was also predicted alongside that of antimonene.^[12] These four 2D materials along with group 14 graphene, silicene, and germanene have opened the door to imagination when it comes to the design of van der Waals heterostructures. As an example, the structural and electronic properties of bilayers composed of group 15 (arsenene/antimonene) and group 14 (graphene/silicene) monolayers have been recently reported.^[23] These bilayers exhibit the expected van der Waals behavior, with soft interlayer elastic constants and small binding energies (**Figure 6**). In these bilayers, the Dirac-like features characteristic of the group 14 layer and the semiconducting features of the group 15 one are well preserved (see an example in **Figure 7d**). This translates into a Schottky contact at this metal-semiconductor interface (Figure 7c). The Schottky barriers are always p-type for the bilayers based on silicene, whereas in the graphene-based ones the interface physics is sensitive to the interlayer distance (Figure 7a,b). The authors of this study also showed that a tensile strain could induce a p-type-to-n-type Schottky barrier transition in the case of the arsenene-graphene bilayer, while a compressive strain would cause a Schottky-to-Ohmic contact transition in the antimonene-graphene one.^[23] In addition, due to a quite inhomogeneous charge redistribution, a band gap is opened at the Dirac point for the antimonene-silicene bilayer, which could be linearly modulated by perpendicular

strain. The versatility and tunability of the electronic characteristics of these hetero-bilayer make them also candidates for novel potential applications in electronics.

In a related work, and also making use of DFT, the combination of germanene and antimonene into bilayer systems was also investigated from the structural, electronic, and optical points of view.^[24] It was found that the monolayers of germanene and antimonene bind to each other via orbital hybridization, which enhances the binding strength. Importantly, a band gap opens due to this hybridization. The authors demonstrated that the AAI pattern (**Figure 8**) has a direct band gap with a value in the vicinity of 0.4 eV, while the other three patterns (also shown in Figure 8) have indirect band gaps ranging from 0.4 to 0.17 eV.

Interestingly, a change in the direction and strength of an external electric field could tune the energy gap in the case of the germanene/antimonene bilayer. This could be achieved over a wide range even to the point of driving a metal-insulator transition. The work function of the bilayer in the AAI stacking, which presents a direct band gap, could be tuned from 3.21 up to 12.33 eV by applying different intensities of the external field. In addition, the germanene/antimonene bilayer was shown to exhibit an optical conductivity larger than that of the individual monolayers.

Vertical stacking of monolayers, while more common and easier to achieve in the laboratory, is not the only possible scheme to create 2D heterostructures. Lateral heterostructures fabricated by 2D building blocks are also opening exciting possibilities in material science and device physics. A novel type of seamless lateral heterostructures formed with alternating pristine arsenene and antimonene (As_nSb_n) has been recently proposed (**Figure 9**).^[25] Their relevant geometric and electronic properties were systematically studied on the basis of DFT calculations as well as their thermal stabilities, finding that these systems can withstand temperatures of 500 K without losing their structural integrity. Phonon analysis also provided evidence for the dynamical stability with the absence of imaginary frequencies. Importantly, direct and reduced energy gaps were also demonstrated. In addition, in plane interfacing

between arsenene and antimonene monolayers causes a type-II alignment 2D heterostructure in which the photo-induced excitons would be confined on both sides of the interline.

Therefore, an efficient separation of electrons and holes can be achieved, which is an appealing feature for optoelectronics, photovoltaics and photocatalysis.

It was also shown that band gap engineering can also be realized through tensile strain modulation with different applied strategies on the heterostructures. The calculated electron and hole effective masses, combined with an estimation of the carrier mobility, not only revealed the potential high charge carrier mobility, which is comparable to that of other 2D materials, but also suggested the assistance to the efficient separation of the excitons. Finally, the authors identified the critical condition ($m/n < 4$) to obtain direct energy gaps and anticipated the end of the monopoly of graphene/h-BN and Transition Metal Dichalcogenides (TMDs) in the preparation of lateral heterostructures.

2.1.7. Transistors based on antimonene

A theoretical and computational analysis of 2D field-effect transistors (FET) based on arsenene and antimonene (**Figure 10**) has been recently reported, where it is demonstrated that these materials are candidates to play a relevant role in devices for digital applications.^[26] Upper estimates of the carrier mobilities in the case of single- and multi-valley studies showed that large phonon-limited mobilities can potentially be obtained both for arsenene and antimonene (a more quantitative analysis is still necessary but can only be carried out when electron-phonon scattering is actually calculated). This result was the main motivation of the investigation of the device performance reported in this work using a multi-scale approach. The main idea was to incorporate the predictive power of DFT calculations into an efficient tight-binding model, which is typically done through the use of maximally localized Wannier functions. When incorporated as channel materials in FETs, both arsenene and antimonene show a performance which is compliant with industry requirements for channel lengths below

10 nm. It is down to this scale that the ultimate atomic thickness of the 2D materials effectively manages to suppress short channel effects and where tunneling starts to play a fundamental role.

2.1.8. Thermoelectric properties

Controlling heat transport through materials design is one important step towards thermal management in 2D materials. It has been argued that a buckled structure is able to suppress heat transport by increasing the flexural phonon (out-of-plane low frequency lattice vibrations) scattering. Somewhat counterintuitive, it has been recently found that, although 2D group 15 materials have a larger mass and higher buckling height than their group 14 counterparts, the calculated thermal conductivity κ is, in general, lower for the latter (**Figure 11**).^[27] A buckled structure is responsible for three conflicting effects: 1) increasing the Debye temperature by the increase of the overlap of the p_z orbitals; 2) suppressing the acoustic-optical scattering by the formation of an acoustic-optical gap; and 3) increasing the flexural phonon scattering. The former two, corresponding to the harmonic phonon part, tend to enhance κ , while the last one, corresponding to the anharmonic part, suppresses it. Interestingly, again based on DFT calculations combined with the Boltzmann transport equation formalism, a recent study^[28] has predicted that antimonene has a low lattice thermal conductivity (actually lower than stanene as shown in Figure 11), which goes as low as $15.1 \text{ W m}^{-1} \text{ K}^{-1}$ at a temperature of 300 K (**Figure 12**). The low thermal conductivity of antimonene originates from the small group velocities of the carriers, low Debye temperature and large buckling height. Moreover, it was also found that the longitudinal acoustic phonon branch dominates the lattice thermal conductivity in the low frequency range, due to its larger mean free path and smaller scattering phase space than those of the transversal and the out-of-plane acoustic branches. A cumulative thermal conductivity analysis indicated that the lattice

thermal conductivity of antimonene can be reduced effectively to $7.56 \text{ W m}^{-1} \text{ K}^{-1}$ through minimizing the sample size down to $9.8 \text{ }\mu\text{m}$.

Finally, in a very recent study^[29] based as well on DFT, thermoelectric factors have been calculated, finding a thermoelectric figure of merit (ZT) of 2.15 at room temperature. ZT is a dimensionless parameter employed to evaluate the performance of thermoelectric materials, being typically around unit. The value obtained for antimonene is the highest ever reported in pristine 2D materials and postulates antimonene as a promising candidate for thermoelectric devices.

2.1.9. Doping

Given the 2D nature of antimonene, doping can be achieved *via* superficial interactions. Chemical doping through tetrathiafulvalene (TTF) and tetracyanoquinodimethane (TCNQ) molecules adsorbed on antimonene was theoretically investigated in Reference^[30] using DFT. The authors found that this chemical route to doping can tune the electrical properties of antimonene. It was also found that the combination of electronic interaction and charge transfer was responsible for an efficient reduction of the band gap, both in the cases of electron-donating (TTF) and electron-accepting (TCNQ) molecules. While an n-type semiconductor (TTF/antimonene) with a deep donor state located at 0.73 eV could be attained, a p-type semiconductor with a shallow acceptor state at 0.27 eV was achieved by TCNQ functionalization. Furthermore, the simultaneous adsorption of TTF and TCNQ on antimonene, both one- and two-sided, yields n-type semiconductors with shallow donor states of 0.15 eV and 0.12 eV, respectively. In conclusion, it is possible to design surface-doped antimonene-based devices, thus broadening the spectrum of applications for this novel 2D semiconductor.

2.1.10. Defects

Defects are inevitably present in materials. Their existence may strongly affect the fundamental physical properties, although not always in a negative manner increasing the functionality of them. This is the case, in particular, for 2D materials. Once again DFT calculations have been performed on antimonene to investigate the formation of Stone-Wales (SW) defects and their effects on its electronic properties.^[31] The formation energy of the SW defect in the buckled lattice structure of antimonene with a large supercell ($6 \times 6 \times 1$), as shown in **Figure 13**, was found to be 1.36 eV, which is even lower than those of SW-defects in silicene and graphene. The calculated values of formation energy and cohesive energy both give insight into the softer bonding nature of antimonene, which results in an easier formation of a SW defect for the freestanding monolayer. From the electronic point of view, the introduction of a SW defect in antimonene breaks the original symmetry and results in a band gap decrease in the band structure. It was also found, not so surprisingly, that the electronic and structural properties of antimonene with SW defects depend on the defect concentration or supercell size. The result of difference charge density reveals that the formation of SW defects in freestanding antimonene inevitably leads to deformations. A STM simulated image of the SW-defected antimonene was also provided, which can help to recognize the SW defect in future experiments.

2.1.11. Strain effects and non-trivial topology

It was early predicted that antimonene undergoes a transition between an indirect and a direct band-gap behavior upon application of a biaxial tensile strain of $\approx 7\%$;^[12a] thereby its potential interest in flexoelectronics. However, before the term antimonene was even coined and maybe of more fundamental interest, theoretical studies had demonstrated that β -antimonene could sustain large (tensile) strain (up to 20%). Band inversion was demonstrated to take place in the vicinity of the Γ point as the strain grows larger than a value that ranges from $\approx 7\%$ to $\approx 18\%$ (**Figure 14**), depending on the calculation details,^[15a, 21, 32] leading to six

Dirac cones within the Brillouin zone. SOC opens up a topologically nontrivial bulk band gap at these Dirac points, and the systems exhibit the features of 2D topological insulators, which are characterized by a nonzero Z_2 topological invariant. The tunable and large bulk band gap, in the range 101-560 meV, makes antimonene a very promising candidate material for the observation of quantum spin Hall effect (QSH) at room temperatures, which is a step forward towards the use of 2D topological insulators in electronic devices with low power consumption. The non-trivial role of SOC also manifests in FL-antimonene, as briefly summarized in the next section.

2.2. Few-layer antimonene

Shortly before antimonene was the focus of attention by the research community, its bulk parent material had also been the subject of an unexpected interest. An elemental bulk material such as antimony happens to be a topological semi-metal on account of an inverted bulk band order.^[10] Despite the absence of a bulk gap, its non-zero topological invariant guarantees that antimony features protected topologically surface states (TSS), but coexisting with bulk bands at the Fermi energy,^[11a, 33] topological effects, originated by strong spin-orbit coupling, are also expected for other monoelemental two dimensional materials as for instance germanene.^[34] Sb(111) in thin film form could become, in principle, a 3D topological insulator if quantum confinement opened a gap in the bulk bands. There is, however, a trade-off here. When the films are thin enough, coupling between TSS on opposite surfaces is expected to degrade or even destroy the TSS exotic properties such as their expected protection against backscattering. Ultimately, a single antimony layer or antimonene even becomes an indirect-gap semiconductor, as discussed in the previous section. Theoretical studies on few-layer antimonene have shown that the decoupling of the TSS requires a minimum of ~ 7 layers.^[11] In between the semiconductor monolayer and the 7-layer antimonene (**Figure 15**) a crossover occurs where claims of the existence of a 2D topological

insulator have also been reported.^[11b] By the time that the TSS are decoupled and the gap at the Dirac point closes down, the Fermi energy crosses the Dirac cone above the Dirac point, but also crosses 6 surface state pockets and 6 bulk pockets.^[33c] The presence of these bulk pockets could prevent the topological nature of the surface states from manifesting in conductivity measurements, although STM studies have shown that backscattering on the surface maintains traces of protection, even for semi-infinite crystals.^[35]

3. Experimental realizations

3.1. Antecedents

Metal films on semiconductors have been long studied (the first results referenced in this review have been published back in the eighties) for an understanding of both the evolution of the films structure up to the bulk phase and the development of properties of the films.

Already in the eighties these studies included the growth of Sb films on various semiconductor substrates, mainly GaAs(110), by filament-type or effusion cell evaporations in ultrahigh vacuum (UHV) conditions, going down to the monolayer case.^[36] However, the electronic properties of such films, studied using Scanning Tunneling Microscopy (STM) and Resonant Raman scattering, are affected by inter-surface coupling, hampering the study of the properties of isolated antimonene layers.

More recently, Sb films were also grown by epitaxial techniques on Bi substrates, either on Bi(111)^[37] or on Bi-terminated Si(111) $\sqrt{3} \times \sqrt{3}$ substrates.^[11a, 33b, 38] In these cases, Angle Resolved Photoemission Spectroscopy (ARPES) and STM were employed to study their electronic properties, focusing mainly on topological aspects. In these surfaces, the electronic states associated with the Sb in contact with the substrate can be substantially modified, preventing as well to obtain further information of the properties of isolated antimonene flakes. A paper published in 2016 reported the growing of Sb films from few- to single- layer on Bi₂Te₂Se substrates.^[39] Their topological behavior was studied by means of STM, but an

hybridized state between conduction bands of the substrate and the Sb film hampered again the study of isolated antimonene layers.

In the last few years other approaches were employed to synthesize Sb in nanostructured forms. Chemical reduction of SbCl_3 on different conditions was carried out to obtain Sb nanocrystals of 10-20 nm size range,^[40] which can be applied to the fabrication of electrodes in Lithium and Sodium batteries.

A plasma-assisted selective reaction approach was also employed to obtain multilayer antimonene as a non-continuous multilayer nanoribbons pile on an InSb surface.^[41] The critical point of this synthesis procedure is the selective reaction induced by large variations of the Gibbs free energy of the involved reactions. Nitrogen ions obtained by radio frequency plasma are implanted near the InSb substrate surface. This way, during a post-annealing, a preferential reaction with indium occurs. Simultaneously, the antimony atoms are segregated out of the surface to form the multilayer antimonene. The photoluminescence response of the synthesized multilayer antimonene was studied, finding a peak that emerged at ~ 610 nm, that was attributed to a turbostratically stacked nanoribbon structure and a quantum confinement effect.

Despite all these efforts, the preparation of isolated few to single layer antimonene was still elusive, and it was not until very recently that it has been demonstrated to be feasible by employing different approaches: micromechanical exfoliation, in which few to single layer flakes are peeled off of bulk antimony using a piece of tape. This method provides the highest quality antimonene crystals, but with a low yield. Liquid phase exfoliation, where layers are obtained inducing a shearing force by sonication of bulk antimony in different solvents. This allows for inexpensive and scalable production of few-layer antimonene. Epitaxial growth methods, in which crystalline layers of antimonene are grown onto different crystalline substrates by depositing antimony atoms. They allow producing significant amounts of single

layer antimonene. These different fabrication methods are presented more in detail in the following sections.

3.2. Micromechanical exfoliation

The well-known “scotch tape method” is the first procedure introduced to isolate 2D films, being used to obtain graphene by repeated peeling of graphite flakes.^[42] Ares *et al.* use a bit more sophisticated version of this technique to isolate antimonene.^[18] Using the standard approach, they found a very little amount of flakes when delaminating antimony. They improved the yield by using a double-step transfer procedure,^[43] based on a first transfer from the adhesive tape to a viscoelastic polymer (Gelfilm from Gelpak®), from which the flakes were transferred to SiO₂/Si substrates. This procedure yielded few-layer flakes with acceptable surface area in a more controlled way, including single-layer antimonene. By means of this approach, micrometer-sized flakes of antimony can be identified by optical microscopy (**Figure 16a**), where the different colors of the terraces reflect different thicknesses. Atomic Force Microscopy (AFM) allows locating smaller and thinner flakes in the surroundings. Figure 16b depicts an AFM topography image of a few-layer antimonene flake, exhibiting a well-defined monolayer terrace at its bottom. Interestingly, this terrace presented a height of ~ 0.9 nm (Figure 16b and c). Similar heights are commonly observed for monolayers in other 2D materials,^[42, 44] suggesting the presence of water underneath the flake which remains captured between the flakes and the SiO₂. The observed rippling is attributed to the conformation of antimonene to the substrate and is very likely not intrinsic as for the case of graphene. As it is commonly done in other 2D materials, Raman spectroscopy was carried out to identify the number of layers of each terrace. Unfortunately, the Raman signal measured for few-layer antimonene flakes adsorbed on SiO₂ is very weak, hampering the final determination of the flake thickness (*vide infra*). Following reference ^[42], single layer graphene terraces can be unambiguously identified by measuring the step height of single

folds. To this end, Ares *et al.* adopted a strategy consisting in an AFM-assisted nanomanipulation, folding the bottom terrace upon the rest of the flake (Figure 16d). The lowest step height of the terrace so folded was about 0.4 nm (inset in Figure 16d and profile in Figure 16e), corresponding to a β -phase antimonene monolayer. The ability to fold without breakage and the angles measured (most of them multiples of 60° , characteristic of a hexagonal atomic lattice) gave evidence of the mechanical stability of monolayer antimonene terraces.

High Resolution Transmission Electron Microscopy (HRTEM), X-ray Energy Dispersive Spectroscopy (XEDS), and high resolution AFM analysis confirmed the high quality of the material and its rhombohedral structure (β -phase).

The stability of the obtained material under ambient conditions was demonstrated by AFM imaging of the same flakes in different time intervals (**Figure 17**). An area with two thin flakes was located just after exfoliation (Figure 17a). The sample was then stored for two months in ambient conditions without any further precaution. The same flakes were then imaged again (Figure 17b), presenting no significant differences. To further confirm stability of the antimonene flakes in the presence of moisture, just after the acquisition of Figure 17b, the sample was immersed in water and new images were acquired (Figure 17c), showing again no significant evolution and presenting a hexagonal periodicity (inset Figure 17c) compatible with the antimony β -phase. The absence of relevant changes is nicely captured in Figure 17d, which shows topography profiles along the lines in Figure 17a-c.

Basic electrical characterization of few-layer antimonene flakes (thicknesses above 6 nm) isolated on gold substrates was also performed using conductive AFM. A linear dependence of the acquired current *vs.* voltage curves was found, in good agreement for thicknesses above two layers, confirming as well the ambient stability of the obtained material.

Since Raman spectroscopy signals on few-layer antimonene on SiO₂ substrates are very weak to be detected, in a later work Ares *et al.* performed a simple and quite accurate identification of the different thicknesses of micromechanically exfoliated flakes on the basis of their optical contrast.^[45] To this end, mechanically exfoliated antimony sheets were isolated on a 300 nm SiO₂/Si substrate.^[18] The optical contrast of flakes was measured using different illumination wavelengths in the visible spectrum and their thicknesses using AFM. **Figure 18** depicts a high-resolution optical micrograph of a representative set of flakes, illuminated using white light (Figure 18a) and under well-defined illumination wavelengths using narrow-bandpass optical filters (Figures 18b-e). The experimental optical contrast was then quantitatively compared with that obtained from a Fresnel law-based model yielding the refractive index and extinction coefficient of these thin crystals in the visible spectrum (**Figure 19a**). From the obtained refractive index, the optical contrast is plotted *versus* the silicon dioxide thickness and the incoming light wavelength (Figure 19b), concluding that the highest optical contrast is observed when using light of wavelengths below 550 nm for substrates with 80 and ~ 240 nm SiO₂ thicknesses. Since Raman spectroscopy signals on few-layer antimonene on SiO₂ substrates are very weak to be detected, this work demonstrates that optical microscopy can be used as a simple tool to identify ultrathin antimonene crystals and to distinguish them from thicker flakes.

3.3. Liquid phase exfoliation

Liquid phase exfoliation (LPE) is a method that has been successfully applied to produce single or few-layers of several 2D-materials in large quantities,^[46] even stable suspensions of few-layer black phosphorus.^[47] The exfoliation of layered materials in liquids is a powerful procedure to give large quantities of dispersed layers suspended in a variety of solvents that, in principle, should allow for mass production. Gibaja *et al.* have demonstrated that high-quality, few-layer antimonene sheets can be obtained by LPE.^[48] Sonication of grinded

antimony crystals in a 4:1 isopropanol-water mixture under ambient conditions and in the absence of any surfactant produces very stable suspensions of micrometer-large few-layer antimonene over weeks. After removing the non-exfoliated material by centrifugation at 3000 rpm (845 rcf) for 3 min, a colorless very stable dispersion showing Faraday-Tyndall effect can be produced. The concentration of these dispersions was *ca.* $1.74 \times 10^{-3} \text{ gl}^{-1}$ as determined by atomic absorption spectrometry (**Figure 20a**). The LPE optimal preparation was determined considering different solvents, sonication experimental conditions and centrifugation parameters. UV/Vis spectroscopy was employed to confirm the stability of the resulting suspensions within time.

AFM images show randomly distributed thin flakes confirming the proper exfoliation of the antimony crystals. Figure 20b depicts a representative topography of few-layer antimonene flakes deposited on a SiO₂/Si substrate. The height histogram analysis of the image (Figure 20c), reveals flakes with step heights multiple of $\sim 4 \text{ nm}$ with average surface areas in the 1-3 μm^2 range. Interestingly, the flakes do not show terraces characteristic of layered 2D materials but well-defined structures presenting heights multiple of $\sim 4 \text{ nm}$. This suggests an apparent mono/bilayer thickness that might correspond to those 4 nm, taken into account that apparent AFM heights of nanosheets produced by LPE can be overestimated due to the presence of residual solvent^[47, 49] as well as contributions from capillary and adhesion forces.^[50]

High resolution AFM and aberration corrected Scanning Transmission Electron Microscopy (STEM) coupled with Electron Energy-Loss Spectroscopy (EELS) were employed to determine the structure and chemical composition of the flakes (**Figure 21**). Figure 21a shows an AFM image with atomic periodicity acquired in a low terrace of the isolated flakes on SiO₂ substrates, in which the atomic periodicity is in excellent accordance with that expected for the antimony β -phase. Figure 21b presents an atomically resolved STEM image of the crystal

structure (80 kV acceleration voltage avoiding beam induced damage), in agreement with that of β -antimony along the $[0 -1 2]$ direction. Figure 21c exhibits compositional maps obtained from the EEL spectra for the Sb M 4,5 and O K absorption edges, presenting a homogeneously distributed Sb signal and little chemical inhomogeneity.

Gibaja *et al.* examined Raman spectroscopy in detail in order to complete the characterization of the isolated few-layer antimonene flakes on SiO₂ substrates. The Raman spectrum of bulk antimony acquired using an excitation wavelength of $\lambda = 532$ nm shows two main phonon peaks: A_{1g} at 150 cm⁻¹ and E_g at 110 cm⁻¹.^[51] Notice that bulk Sb β -phase consists of buckled quasi-2D layers in an ABC-type sequence (space group $R\bar{3}m$), presenting three Raman active optical modes: two degenerate modes of E_g symmetry (experimentally observed at *ca.* 100 cm⁻¹), corresponding to the in-plane transversal and longitudinal vibrations of the sublayers in opposed directions. On the other hand, the third mode generates a Raman peak at 150 cm⁻¹, which is related to opposite in-phase out-of-plane vibrations of the sublayers having A_{1g} symmetry (**Figure 22**). The correlation of statistical Raman microscopy (SRM) and AFM imaging in a polydisperse sample revealed that flakes exhibiting apparent thicknesses below ~ 70 nm show very weak Raman signals. In particular, it shows a decrease of the peaks intensities as well as a slight blue shift with the thickness, already observed on micromechanically-exfoliated antimony sheets (Figure 22).^[18] Moreover, no Raman features could be measured even using other laser excitation wavelengths: $\lambda_{\text{ex}} = 785, 633, 532, 473, 457,$ and 405 nm. Theoretical phonon spectra calculations, carried out to understand this experimental observation, indicate two interesting behaviors. On one side, a significant shrinkage of the in-plane lattice constant of the FL-antimonene compared to the bulk material when the thickness of the layers is decreased to a trilayer, bilayer, and monolayer (from $a = 4.3$ Å for the bulk, to $a = 4.01$ Å for the monolayer). As a result, for the monolayer, the frequency of the bulk E_g mode exhibits an increase from 88 to 167 cm⁻¹, and the bulk A_{1g}

mode is also blue-shifted when decreasing the thickness. On the other side, the DFT calculations predicted a decrease of *ca.* three orders of magnitude from bulk to monolayer Sb, providing a hint on the experimentally observed absence of Raman signals in the case of the thinnest flakes (Figure 22).

Recently, Gu *et al.* have developed the LPE of antimonene using an isopropanol solution with a constant concentration of NaOH.^[52] In this work, Sb nanosheets with minimum thicknesses comprised in the 3.0–4.3 nm range were obtained after sonicating the samples during 30 h and centrifuging at 2000 rpm to eliminate aggregates. Moreover, they used these suspensions to synthesize reduced graphene oxide/antimonene (rGO/Sb) hybrid materials of interest in sodium-ion batteries, exhibiting a high volumetric capacity of 1226 mA h cm⁻³, high-rate capability and good cycle performance (**Figure 23**).

More recently, Gusmão *et al.* have obtained As, Sb and Bi exfoliated nanosheets by liquid phase exfoliation using rotating blades mixers.^[53] In this work, bulk crystals of antimony were exfoliated in aqueous surfactant sodium cholate using two types of kitchen blenders without the need of purged media or the use of a glove box. Using this approach, liquid phase exfoliated nanosheets in suspension were obtained. Dynamic light scattering measurements indicated a broad size distribution ranging 100 - 900 nm with maxima around 200 nm. Electrochemical measurements using the resulting material as electrode were carried out, showing that the shear exfoliation induces new activated edges that improve electrode response compared to bulk. Potential energy related applications were evaluated by testing their catalytic activity in the hydrogen evolution reaction (HER), oxygen evolution reaction (OER) and oxygen reduction reaction (ORR), showing that antimony nanosheets are a wide pH range catalyst for HER.

3.4. Epitaxial growth methods

Epitaxial growth methods typically refer to the deposition of a crystalline layer onto a crystalline substrate. The micromechanical exfoliation technique provides the highest quality 2D materials layers and a proof of concept for the existence of antimonene. However, large quantity synthesis using this procedure is not feasible. On the contrary, epitaxial synthesis is a well-known scalable method to produce significant amounts of crystalline 2D materials. It has been employed under different approaches to produce few-layer antimonene down to the single-layer regime.

3.4.1. Molecular Beam Epitaxy

Molecular Beam Epitaxy (MBE) was successfully employed by Lei *et al.*^[54] and Wu *et al.*^[55] to grow antimonene onto Bi₂Te₃ and Sb₂Te₃ substrates, and PdTe₂ substrates respectively. Those surfaces were chosen because antimonene can grow smoothly on them with small lattice mismatches.

Lei *et al.* prepared antimonene by depositing Sb on the Bi₂Te₃ and Sb₂Te₃ substrates at room temperature in UHV conditions.^[54] Low-Energy Electron Diffraction (LEED) patterns indicate the 1x1 periodicity showing that high-quality epitaxial films were formed. The electronic structure of the grown films was probed by ARPES measurements, indicating that lattice distortion and charge transfer effect induce a change in surface-state band dispersion. Wu *et al.* reported the growth of monolayer antimonene on a 2D layered PdTe₂ substrate by evaporating Sb atoms onto a freshly cleaved PdTe₂ substrate, kept at 400 K.^[55] **Figure 24a** depicts a schematic of the growth process. Figure 24b shows a Scanning Tunneling Microscopy (STM) image of a large atomically smooth antimonene film with a well-defined LEED pattern corresponding to the 1x1 orientation (inset). STM atomic resolution images (Figure 24c) show the graphene-like honeycomb lattice with a buckled configuration, as expected for the antimonene β -phase. The apparent height of the antimonene layer is ~ 2.8 Å (Figure 24d), as measured by the profile line across the edge of the antimonene film

(corresponding to the red line in Figure 24b). This height is close to that of a single layer of antimonene in the Sb bulk, indicating that the antimony adlayer is a monolayer. Figure 24e corresponds to the height profile of the buckled honeycomb lattice along the blue line in Figure 24c. It indicates a periodicity of 4.13 ± 0.02 Å in the lattice, a value quite close to the periodicity of the PdTe₂ substrate (4.10 ± 0.02 Å) consistent with the LEED pattern showing (1x1) diffraction points.

X-ray Photoelectron Spectroscopy (XPS) data acquired on these samples indicated that there is no chemical interfacial coupling between the antimonene and the PdTe₂ substrate, being the interaction between monolayer antimonene and the substrate via a weak van der Waals force. Air-stability of monolayer antimonene was also studied by exposing the sample to ambient conditions for 20 min. STM images of antimonene islands were acquired before and after exposition (**Figure 25**) showing no substantial contamination, confirming the environmental stability of the antimonene. XPS measurements were also performed, resulting in no chemical reaction of the antimony during air exposure.

Very recently, Fortin-Deschênes *et al.* have carried out the growth of bidimensional single to few-layer antimonene by evaporating antimony crystals onto a technological relevant substrate such as Ge(111).^[56] The authors reported a detailed study with different characterization techniques including, low energy electron diffraction and microscopy (LEED and LEEM), STM, TEM, X-ray photoemission spectroscopy and microscopy (XPS and XPEEM) and Raman spectroscopy, combined with DFT simulations. The authors confirm the air ambient stability of the so growth layers. Interestingly, electrical characterization showed the single antimonene layer to be semimetallic, therefore preventing determination of the electronic band gap expected for isolated monolayers of antimonene.

3.4.2. van der Waals Epitaxy

The van der Waals epitaxy technique relies in the use of substrates without dangling bonds on their surface. The epitaxial grown layers are connected with the substrates through weak van der Waals interaction instead of strong chemical bonding, enabling the epitaxial growth of layered materials with different crystalline symmetry to the substrate.

Recently, Ji *et al.* were able to synthesize high-quality β -phase few-layer antimonene polygons using this technique on a variety of substrates, including fluorophlogopite mica ($\text{KMg}_3(\text{AlSi}_3\text{O}_{10})\text{F}_2$) and flexible supports.^[57] The fabrication process makes use of a two-zone tube furnace with separate temperature controls. **Figure 26a** depicts a schematic illustration of the synthesis procedure. Antimony powder was placed in the T_1 zone and heated up to 660 °C to generate antimony vapor. The substrates are placed in the T_2 zone of the furnace with a typical temperature of 380 °C, producing antimony condensation. A transporting flow of $\text{Ar}+\text{H}_2$ gas was used to transfer antimony vapor from the T_1 to the T_2 area originating a soft-landing and diffusion of Sb atoms on the substrate, allowing crystal growth (Figure 26b). This crystallization process on mica can be split into nucleation and lateral growth. At a first stage, the antimony vapors carried by the $\text{Ar}+\text{H}_2$ gas cool down and form nuclei on the mica substrate. Then, Sb adatoms on mica diffuse to the edge of the initial nuclei, growing fast into layers along the chemically passivated surface. The synthesis process was kept for 60 min and then the furnace temperature was lowered to room temperature. In particular, mica, an atomically flat substrate, was found to be a very suitable platform for van der Waals epitaxy growth of few-layer antimonene thanks to the absence of dangling bonds on its surface. Optical microscopy imaging (Figure 26c-f) reveals the formation of different few-layer antimonene polygons shapes, including triangles, hexagons, rhombus and trapezoids. Growth using silicon and sapphire substrates was also possible, but irregular microstructures were observed. The absence of dangling bonds seems to be crucial for the successful growth, which is confirmed by XPS.

The majority of the polygons have lateral sizes around 5-10 μm . AFM measurements provide polygons thickness values down to 4 nm (~ 10 atomic layers, Figure 26g), and even a very small and irregular sheet with lateral size around 100 nm presenting a thickness down to ~ 1 nm was found (Figure 26h), characteristic of monolayer antimonene.^[18]

A battery of techniques, including HRTEM, STEM, energy dispersive spectroscopy (EDS) and selected area electron diffraction (SAED) were used to identify the chemical composition and crystal structure of the synthesized material, confirming its crystallinity, high quality as well as corroborating its rhombohedral structure (β -phase). β -phase formation was also confirmed by Raman spectroscopy. Interestingly, the E_g and A_{1g} Raman peaks observed for the monocrystalline antimonene layers show the intensity dependence reported for few-layer antimonene obtained by micromechanical exfoliation and LPE,^[18, 48] but remarkably the signal detection on mica is significantly enhanced in comparison to that observed on SiO_2 . Moreover, a phonon softening effect (blue shift) was observed when the sample thickness decreases from bulk to 5 nm, *i.e.* the E_g peak frequency increases from 110.7 cm^{-1} to 138.7 cm^{-1} and the A_{1g} peak frequency increases from 149.2 to 166.4 cm^{-1} . A similar behavior has been observed for LPE exfoliated antimonene^[48, 52] and other related 2D materials.^[46, 58] This softening of the optical phonons is probably attributed to the shrink of the lattice constant associated with the decreasing number of layers and/or long-range Coulombic interlayer interactions.^[57] Stability of the multilayer antimonene samples prepared by van der Waals epitaxy to ambient conditions was confirmed by optical microscopy, AFM, Raman and EDS (**Figure 27**).

Transistor-like devices were fabricated using few-layer antimonene polygons with thicknesses of 30, 40 and 50 nm grown on mica, depositing Cr/Au as contact electrodes and hafnium oxide as a top gate dielectric. From these devices the electrical conductivity of the few-layer antimonene polygons was calculated to be $1.6 \times 10^4\text{ S m}^{-1}$, a typical conductivity value for semimetals, which remained stable after a series of bending experiments performed thanks to

the flexibility of the mica substrates. Additionally, the samples also showed good optical transparency in the visible light range.

3.5. Antimonene quantum dots

Antimonene quantum dots (AQDs) have been recently fabricated by Lu *et al.*^[59] and Tao *et al.*^[60] using a sonochemical exfoliation approach. This technique is based on ultrasound probe sonication combined with ice-bath sonication of Sb powder in a solvent: N-methyl-2-pyrrolidone (NMP) in reference^[59] or ethanol in reference^[60]. **Figure 28a** depicts a schematic illustration of the synthesis procedure. Both ultrasound probe sonication and ice-bath sonication last for several hours (5 to 10 h, depending on the experimental set-up). The resulting solution was then centrifuged. In this way, uniform and small particles can be achieved in a high yield. Figures 28b-e present the characterization of the obtained AQDs using NMP as a solvent. AFM measurements result in an average height about 3.2 nm (Figure 28b-c), TEM images provide an average size around 3.4 nm (Figure 28d) and Raman spectroscopy shows the two peaks characteristic of antimonene (Figure 28e). **Figure 29** shows the characterization of the AQDs obtained using ethanol as a solvent. TEM and AFM images showed an average size of ~ 2.8 nm and an average thickness of ~ 1.6 nm. Raman spectroscopy and XPS were also employed to confirm the AQDs composition.

Lu *et al.* also synthesized few-layer antimonene flakes through an electrochemically exfoliation approach and studied both AQDs and few-layer flakes nonlinear optical Kerr response at the visible band by using the spatial self-phase modulation (SSPM) measurement technique.^[59] By using this methodology, they observed a strong nonlinear optical response, estimating the nonlinear refraction index of antimonene to be $\sim 10^{-5} \text{ cm}^2 \text{ W}^{-1}$. The obtained results point to antimonene as a new kind of promising optical Kerr material with enhanced stability, making it a good candidate for the fabrication of photonics devices such as detectors, passive Q-switchers or light modulators.

AQDs coated with 1,2-distearoyl-sn-glycero-3-phosphoethanolamine-N-[methoxy(poly ethylene glycol)] (DSPE-PEG) to enhance dispersity in physiological medium,^[60] were employed as photothermal agents for cancer therapy due to their high photothermal conversion efficacy (PTCE). The PEG-coated AQDs exhibited a PTCE of 45.5 %, higher than many other photothermal agents based on nanomaterials such as graphene, Au, MoS₂ and black phosphorus, excellent stability in physiological conditions, superior near infrared (NIR) photothermal performance and no obvious toxicity. More importantly, they also presented excellent NIR light-induced tumor ablation and biocompatibility *in vivo*. **Figure 30** summarizes *in vivo* therapeutic studies and biocompatibility evaluations carried out on MCF-7 tumor-bearing mice under different treatments: saline (G1), NIR irradiation (G2), PEG-coated AQDs (G3), or PEG-coated AQDs with subsequent NIR irradiation (G4) after intratumor injection. Tumors treated with PEG-coated AQDs and NIR irradiation were ablated with negligible growth or no regrowth. This study paves the way for the development of antimonene-based biomedical applications.

3.6. Chemical functionalization

Chemical functionalization is a promising route to controllably engineer the band gap structure, create novel architectures and manipulate the interfacial characteristics of 2D materials, improving its processability and applications. Indeed, as shown in the previous section, functionalized antimonene quantum dots were explored for its application in biomedicine.^[60] Moreover, chemical functionalization represents an avenue worth to be explored for tailoring electronic properties, such as controlling doping levels and charge carrier concentrations. It is expected that chemical methods will allow a fine-tuning of the properties of antimonene just as it has been developed for graphene or other 2D materials such as BP or transition metal chalcogenides, thereby enabling the development of device applications.^[61]

The chemical functionalization –and therefore the molecular doping– of antimonene remains almost unexplored. In a related precedent, Abellán *et al.* recently reported on the non-covalent functionalization of BP with electron-poor and polarizable polycyclic aromatic molecules, observing a remarkable charge-transfer behavior, and dramatically improving the resistance of the flakes against oxygen degradation.^[62] By following the same approach, the non-covalent functionalization of antimonene with a perylene bisimide (PDI) has been recently reported for the first time (**Figure 31**) showing a more pronounced charge-transfer behavior than BP.^[63] Indeed, scanning Raman microscopy and statistical Raman spectroscopy revealed the preferential supramolecular functionalization of the antimonene flakes deposited on Si/SiO₂ substrates with a substantial quenching of the PDI fluorescence. Scanning photoelectron microscopy and computational studies demonstrated the nature of the strong noncovalent interaction between PDI and antimonene as well as the significant charge-transfer from the antimonene to the PDI, which resulted to be *ca.* twice as large as that observed for BP. DFT calculations indicate that the non-covalent functionalization of antimonene gives rise to a charge-transfer band gap of about 1.05 eV, being a promising route for tailoring its electronic properties. Interestingly, the scanning photoelectron microscopy revealed the formation of a spontaneous passivation layer in pristine antimonene under environmental conditions, which is expected to provide an excellent stability to the flakes. As a matter of fact, the formation of 2D antimonene oxides having tunable direct band gaps and small effective electron mass – indicative of high carrier mobility– have been theoretically predicted.^[64] This novel family of materials holds a 2D topological insulator behavior with a sizable global band gap of 177 meV, characterized by the nontrivial Z_2 topological invariant and the topological edge states. Finally, in order to determine the compatibility of this supramolecular functionalization approach with devices fabrication, studies on PDI adlayer removal from the antimonene surface have been carried out. Thus, it has been determined that desorption of the PDI molecules takes place at 300-350 °C. This is reflected in a simultaneous decrease of the

intensity of the characteristic PDI Raman peaks, as well as a concomitant intensification of the fluorescence background. AFM studies also confirm that at 300 °C the PDI molecules are partially removed, and further increasing the temperature to 400 °C produces the elimination of the adlayer from the antimonene surface. This reversible supramolecular functionalization exemplifies an advantage compared to black phosphorus and paves the way for the thermal annealing of antimonene flakes in the preparation of devices. It is expected that these results will provide an impetus in the research of antimonene chemical modification.

4. Conclusions

Antimonene is, among the newly discovered 2D materials, widely acclaimed as one of their most promising members because of their predicted physical properties and its extremely high chemical stability that enables many potential applications. Theoretical works anticipated a number of exciting physicochemical properties, including a tunable band gap with potential applications in optoelectronics, low thermal conductance with low electrical resistivity (suggesting energy generation through thermoelectricity), and exotic topological features. Its strong spin-orbit coupling along with the semimetallic character of the parent bulk antimony are responsible, in theory, for a wealth of different electronic behaviors upon changing the number of layers. This sets antimonene apart from most other 2D crystals where the change in the number of layers mostly affects only the magnitude and nature of the gap. Being this important, the transition from an indirect-gap semiconductor (monolayer) through a possible 2D topological insulator (3-4 layers) to a 3D topological semimetal (more than 7 layers), gives such a broad spectrum of behaviors to such a simple elemental material that is hard to imagine all the possible applications. Fortunately, over the past year a few experimental works made all those expectations somewhat closer to reality. First of all, it was demonstrated that it is possible to isolate very stable monolayers of antimonene under environmental

conditions.^[18] In addition, new experimental procedures such as liquid phase exfoliation^[48] and epitaxial growth^[54-55] methods have been also reported.

Some of the first reported physical properties of antimonene are very appealing. Thus, LPE has provided the realization of antimonene quantum dots showing a remarkable nonlinear refraction index of $\sim 10^{-5} \text{ cm}^2 \text{ W}^{-1}$ making them excellent candidates for the fabrication of photonics devices such as detectors, passive Q-switchers or light modulators.^[59] Additionally, graphene oxide/antimonene hybrid material has shown a high volumetric capacity of 1226 mA h cm^{-3} , high-rate capability and good cycle performance potentially useful for sodium-ion batteries fabrication.^[52]

Importantly, reversible supramolecular chemical functionalization has also been demonstrated. This possibility enables the modulation of the antimonene band gap, creating novel architectures and manipulating its interfacial characteristics, improving its processability. Indeed coated AQDs have recently been produced showing remarkable *in vivo* NIR light-induced tumor ablation and biocompatibility.^[60] This seminal result opens unexpected avenues for antimonene in biomedicine. However, we aware that covalent chemical functionalization will also bring new scenarios towards applications in many fields. Characterization of the obtained material was already reported, although a clear-cut experiment measuring the electronic gap and the transport properties of a single layer of antimonene obtained by mechanical exfoliation is still lacking. Therefore, there is great need for experimental data of its band gap to narrow the large theoretical scatter in its value. A positive result in future experiments will certainly trigger even further the interest for this new material. Work on these topics and in the potential applications of antimonene is surely now in progress in many laboratories.

Acknowledgements

We thank financial support from the Spanish Ministerio de Economía y Competitividad through the “María de Maeztu” Programme for Units of Excellence in R&D (MDM-2014-0377) and the projects MAT2016-77608-C3-1-P and -C3-3-P, and FIS2016-80434-P. We also acknowledge the European Union structural funds and the Comunidad de Madrid under grant MAD2D No. S2013/MIT-3007, the Generalitat Valenciana under grant No. PROMETEO/2012/011, and the Fundación Ramón Areces. The research leading to these results was partially funded by the European Union Seventh Framework Programme under grant agreement No. 604391 Graphene Flagship. We thank the Deutsche Forschungsgemeinschaft (DFG-SFB 953 “Synthetic Carbon Allotropes”, Project A1) for financial support. G.A. thanks the FAU for the Emerging Talents Initiative (ETI) grant #WS16-17_Nat_04.

Received: ((will be filled in by the editorial staff))

Revised: ((will be filled in by the editorial staff))

Published online: ((will be filled in by the editorial staff))

References

- [1] K. S. Novoselov, A. K. Geim, S. V. Morozov, D. Jiang, Y. Zhang, S. V. Dubonos, I. V. Grigorieva, A. A. Firsov, *Science* **2004**, 306, 666.
- [2] A. K. Geim, K. S. Novoselov, *Nat. Mater.* **2007**, 6, 183.
- [3] a) Q. Tang, Z. Zhou, *Prog. Mater. Sci.* **2013**, 58, 1244; b) Q. Tang, Z. Zhou, Z. F. Chen, *Wires Comput. Mol. Sci.* **2015**, 5, 360; c) R. Mas-Balleste, C. Gomez-Navarro, J. Gomez-Herrero, F. Zamora, *Nanoscale* **2011**, 3, 20.
- [4] a) A. K. Geim, *Science* **2009**, 324, 1530; b) K. S. Novoselov, V. I. Fal'ko, L. Colombo, P. R. Gellert, M. G. Schwab, K. Kim, *Nature* **2012**, 490, 192; c) A. C. Ferrari, F. Bonaccorso, V. Fal'ko, K. S. Novoselov, S. Roche, P. Boggild, S. Borini, F. H. L. Koppens, V. Palermo, N. Pugno, J. A. Garrido, R. Sordan, A. Bianco, L. Ballerini, M. Prato, E. Lidorikis, J. Kivioja, C. Marinelli, T. Ryhanen, A. Morpurgo, J. N. Coleman, V. Nicolosi, L. Colombo, A. Fert, M. Garcia-Hernandez, A. Bachtold, G. F. Schneider, F. Guinea, C. Dekker, M. Barbone, Z. P. Sun, C. Galiotis, A. N. Grigorenko, G. Konstantatos, A. Kis, M. Katsnelson, L. Vandersypen, A. Loiseau, V. Morandi, D. Neumaier, E. Treossi, V. Pellegrini, M. Polini, A. Tredicucci, G. M. Williams, B. H. Hong, J. H. Ahn, J. M. Kim, H. Zirath, B. J. van Wees, H. van der Zant, L. Occhipinti, A. Di Matteo, I. A. Kinloch, T. Seyller, E. Quesnel, X. L. Feng, K. Teo, N.

- Rupesinghe, P. Hakonen, S. R. T. Neil, Q. Tannock, T. Lofwander, J. Kinaret, *Nanoscale* **2015**, 7, 4598; d) M. Chhowalla, H. S. Shin, G. Eda, L. J. Li, K. P. Loh, H. Zhang, *Nat. Chem.* **2013**, 5, 263; e) Q. Wang, D. O'Hare, *Chem. Rev.* **2012**, 112, 4124.
- [5] Q. H. Wang, K. Kalantar-Zadeh, A. Kis, J. N. Coleman, M. S. Strano, *Nat. Nanotechnol.* **2012**, 7, 699.
- [6] C. Tan, H. Zhang, *Chem. Soc. Rev.* **2015**, 44, 2713.
- [7] A. Castellanos-Gomez, *J. Phys. Chem. Lett.* **2015**, 6, 4873.
- [8] Y. Huang, J. Qiao, K. He, S. Bliznakov, E. Sutter, X. Chen, D. Luo, F. Meng, D. Su, J. Decker, W. Ji, R. S. Ruoff, P. Sutter, *Chem. Mater.* **2016**, 28, 8330.
- [9] a) G. Abellán, S. Wild, V. Lloret, N. Scheuschner, R. Gillen, U. Mundloch, J. Maultzsch, M. Varela, F. Hauke, A. Hirsch, *J. Am. Chem. Soc.* **2017**, 139, 10432; b) J. O. Island, G. A. Steele, H. S. J. van der Zant, A. Castellanos-Gomez, *2D Mater.* **2015**, 2, 011002.
- [10] L. Fu, C. L. Kane, *Phys. Rev. B* **2007**, 76, 045302.
- [11] a) G. Bian, X. Wang, Y. Liu, T. Miller, T. C. Chiang, *Phys. Rev. Lett.* **2012**, 108, 176401; b) P. Zhang, Z. Liu, W. Duan, F. Liu, J. Wu, *Phys. Rev. B* **2012**, 85, 201410(R).
- [12] a) S. Zhang, Z. Yan, Y. Li, Z. Chen, H. Zeng, *Angew. Chem. Int. Ed.* **2015**, 54, 3112; b) S. L. Zhang, M. Q. Xie, F. Y. Li, Z. Yan, Y. F. Li, E. J. Kan, W. Liu, Z. F. Chen, H. B. Zeng, *Angew. Chem. Int. Ed.* **2016**, 55, 1666.
- [13] G. Wang, R. Pandey, S. P. Karna, *ACS Appl. Mater. Interfaces* **2015**, 7, 11490.
- [14] O. U. Akturk, V. O. Ozcelik, S. Ciraci, *Phys. Rev. B* **2015**, 91, 235446.
- [15] a) Z.-Q. Huang, C.-H. Hsu, F.-C. Chuang, Y.-T. Liu, H. Lin, W.-S. Su, V. Ozolins, A. Bansil, *New J. Phys.* **2014**, 16, 105018; b) H. Lu, J. Gao, Z. Hu, X. Shao, *RSC Adv.* **2016**, 6, 102724; c) A. N. Rudenko, M. I. Katsnelson, R. Roldán, *Phys. Rev. B* **2017**, 95, 081407; d) D. Singh, S. K. Gupta, Y. Sonvane, I. Lukacevic, *J. Mater. Chem. C* **2016**, 4, 6386; e) Y. Wang, P. Huang, M. Ye, R. Quhe, Y. Pan, H. Zhang, H. Zhong, J. Shi, J. Lu, *Chem. Mater.* **2017**, 29,

- 2191; f) M. Xie, S. Zhang, B. Cai, Z. Zhu, Y. Zou, H. Zeng, *Nanoscale* **2016**, 8, 13407; g) Y. Xu, B. Peng, H. Zhang, H. Shao, R. Zhang, H. Zhu, *Ann. Phys.* **2017**, 529, 1600152.
- [16] A. Castellanos-Gomez, L. Vicarelli, E. Prada, J. O. Island, K. L. Narasimha-Acharya, S. I. Blanter, D. J. Groenendijk, M. Buscema, G. A. Steele, J. V. Alvarez, H. W. Zandbergen, J. J. Palacios, H. S. J. van der Zant, *2D Mater.* **2014**, 1, 025001.
- [17] a) O. U. Akturk, E. Akturk, S. Ciraci, *Phys. Rev. B* **2016**, 93, 035450; b) R.-S. Meng, M. Cai, J.-K. Jiang, Q.-H. Liang, X. Sun, Q. Yang, C.-J. Tan, X.-P. Chen, *IEEE Electron Device Lett.* **2017**, 38, 134.
- [18] P. Ares, F. Aguilar-Galindo, D. Rodríguez-San-Miguel, D. A. Aldave, S. Díaz-Tendero, M. Alcamí, F. Martín, J. Gómez-Herrero, F. Zamora, *Adv. Mater.* **2016**, 28, 6332.
- [19] Y. Wang, Y. Ding, *Nanoscale Res. Lett.* **2015**, 10, 254.
- [20] J. J. Palacios, J. Fernandez-Rossier, L. Brey, H. A. Fertig, *Semicond. Sci. Technol.* **2010**, 25, 033003.
- [21] F.-C. Chuang, C.-H. Hsu, C.-Y. Chen, Z.-Q. Huang, V. Ozolins, H. Lin, A. Bansil, *Appl. Phys. Lett.* **2013**, 102, 022424.
- [22] C. Sabater, D. Gosalbez-Martinez, J. Fernandez-Rossier, J. G. Rodrigo, C. Untiedt, J. J. Palacios, *Phys. Rev. Lett.* **2013**, 110, 176802.
- [23] Y. Wang, Y. Ding, *Phys. Chem. Chem. Phys.* **2015**, 17, 27769.
- [24] X. Chen, Q. Yang, R. Meng, J. Jiang, Q. Liang, C. Tan, X. Sun, *J. Mater. Chem. C* **2016**, 4, 5434.
- [25] Q. Sun, Y. Dai, Y. Ma, N. Yin, W. Wei, L. Yu, B. Huang, *2D Mater.* **2016**, 3, 035017.
- [26] G. Pizzi, M. Gibertini, E. Dib, N. Marzari, G. Iannaccone, G. Fiori, *Nat. Commun.* **2016**, 7, 12585.
- [27] B. Peng, D. Zhang, H. Zhang, H. Shao, G. Ni, Y. Zhu, H. Zhu, *Nanoscale*, **2017**, 9, 7397.
- [28] S. Wang, W. Wang, G. Zhao, *Phys. Chem. Chem. Phys.* **2016**, 18, 31217.

- [29] K.-X. Chen, S.-S. Lyu, X.-M. Wang, Y.-X. Fu, Y. Heng, D.-C. Mo, *J. Phys. Chem. C* **2017**, *121*, 13035.
- [30] M. Xie, S. Zhang, B. Cai, Y. Zou, H. Zeng, *RSC Adv.* **2016**, *6*, 14620.
- [31] Y. Hu, Y. Wu, S. Zhang, *Phys. B* **2016**, *503*, 126.
- [32] a) X. Wu, X. Zhang, X. Wang, Z. Zeng, *AIP Adv.* **2016**, *6*, 045318; b) M. Zhao, X. Zhang, L. Li, *Sci. Rep.* **2015**, *5*, 16108.
- [33] a) H. M. Benia, C. Strasser, K. Kern, C. R. Ast, *Phys. Rev. B* **2015**, *91*, 161406(R); b) G. Bian, T. Miller, T. C. Chiang, *Phys. Rev. Lett.* **2011**, *107*, 036802; c) D. Hsieh, Y. Xia, L. Wray, D. Qian, A. Pal, J. H. Dil, J. Osterwalder, F. Meier, G. Bihlmayer, C. L. Kane, Y. S. Hor, R. J. Cava, M. Z. Hasan, *Science* **2009**, *323*, 919.
- [34] A. Acun, L. Zhang, P. Bampoulis, M. Farmanbar, A. van Houselt, A. N. Rudenko, M. Lingenfelder, G. Brocks, B. Poelsema, M. I. Katsnelson, H. J. W. Zandvliet, *J. Phys.: Condens. Matter* **2015**, *27*, 443002.
- [35] J. Seo, P. Roushan, H. Beidenkopf, Y. S. Hor, R. J. Cava, A. Yazdani, *Nature* **2010**, *466*, 343.
- [36] a) R. M. Feenstra, P. Martensson, *Phys. Rev. Lett.* **1988**, *61*, 447; b) P. Martensson, R. M. Feenstra, *Phys. Rev. B* **1989**, *39*, 7744; c) W. Richter, N. Esser, A. Kelnberger, M. Kopp, *Solid State Commun.* **1992**, *84*, 165; d) C. K. Shih, R. M. Feenstra, P. Martensson, *J. Vac. Sci. Technol., A* **1990**, *8*, 3379.
- [37] H. Höchst, C. R. Ast, *J. Electron Spectrosc. Relat. Phenom.* **2004**, *137–140*, 441.
- [38] G. Yao, Z. Luo, F. Pan, W. Xu, Y. P. Feng, X.-s. Wang, *Sci. Rep.* **2013**, *3*, 2010.
- [39] S. H. Kim, K.-H. Jin, J. Park, J. S. Kim, S.-H. Jhi, H. W. Yeom, *Sci. Rep.* **2016**, *6*, 33193.
- [40] a) M. He, K. Kravchyk, M. Walter, M. V. Kovalenko, *Nano Lett.* **2014**, *14*, 1255; b) M. Walter, R. Erni, M. V. Kovalenko, *Sci. Rep.* **2015**, *5*, 8418.

- [41] H.-S. Tsai, C.-W. Chen, C.-H. Hsiao, H. Ouyang, J.-H. Liang, *Chem. Commun.* **2016**, 52, 8409.
- [42] K. S. Novoselov, A. K. Geim, S. V. Morozov, D. Jiang, Y. Zhang, S. V. Dubonos, I. V. Grigorieva, A. A. Firsov, *Science* **2004**, 306, 666.
- [43] A. Castellanos-Gomez, M. Buscema, S. J. van der Zant Herre, G. A. Steele, *2D Mater.* **2014**, 1, 011002.
- [44] J. Israelachvili, *Intermolecular and Surface Forces*, Academic Press, London **1991**.
- [45] P. Ares, F. Zamora, J. Gomez-Herrero, *ACS Photonics* **2017**, 4, 600.
- [46] a) J. N. Coleman, M. Lotya, A. O'Neill, S. D. Bergin, P. J. King, U. Khan, K. Young, A. Gaucher, S. De, R. J. Smith, I. V. Shvets, S. K. Arora, G. Stanton, H.-Y. Kim, K. Lee, G. T. Kim, G. S. Duesberg, T. Hallam, J. J. Boland, J. J. Wang, J. F. Donegan, J. C. Grunlan, G. Moriarty, A. Shmeliov, R. J. Nicholls, J. M. Perkins, E. M. Grieveson, K. Theuwissen, D. W. McComb, P. D. Nellist, V. Nicolosi, *Science* **2011**, 331, 568; b) V. Nicolosi, M. Chhowalla, M. G. Kanatzidis, M. S. Strano, J. N. Coleman, *Science* **2013**, 340, 1226419.
- [47] D. Hanlon, C. Backes, E. Doherty, C. S. Cucinotta, N. C. Berner, C. Boland, K. Lee, A. Harvey, P. Lynch, Z. Gholamvand, S. F. Zhang, K. P. Wang, G. Moynihan, A. Pogle, Q. M. Ramasse, N. McEvoy, W. J. Blau, J. Wang, G. Abellan, F. Hauke, A. Hirsch, S. Sanvito, D. D. O'Regan, G. S. Duesberg, V. Nicolosi, J. N. Coleman, *Nat. Commun.* **2015**, 6, 8563.
- [48] C. Gibaja, D. Rodriguez-San-Miguel, P. Ares, J. Gómez-Herrero, M. Varela, R. Gillen, J. Maultzsch, F. Hauke, A. Hirsch, G. Abellán, F. Zamora, *Angew. Chem. Int. Ed.* **2016**, 55, 14345.
- [49] K. R. Paton, E. Varrla, C. Backes, R. J. Smith, U. Khan, A. O'Neill, C. Boland, M. Lotya, O. M. Istrate, P. King, T. Higgins, S. Barwich, P. May, P. Puczkarski, I. Ahmed, M. Moebius, H. Pettersson, E. Long, J. Coelho, S. E. O'Brien, E. K. McGuire, B. M. Sanchez, G. S. Duesberg, N. McEvoy, T. J. Pennycook, C. Downing, A. Crossley, V. Nicolosi, J. N. Coleman, *Nat. Mater.* **2014**, 13, 624.

- [50] P. Nemes-Incze, Z. Osvath, K. Kamaras, L. P. Biro, *Carbon* **2008**, *46*, 1435.
- [51] X. Wang, K. Kunc, I. Loa, U. Schwarz, K. Syassen, *Phys. Rev. B* **2006**, *74*, 134305.
- [52] J. Gu, Z. Du, C. Zhang, J. Ma, B. Li, S. Yang, *Adv. Energy Mater.* **2017**, 1700447.
- [53] R. Gusmão, Z. Sofer, D. Bouša, M. Pumera, *Angew. Chem. Int. Ed.*,
DOI:10.1002/anie.201706389.
- [54] T. Lei, C. Liu, J.-L. Zhao, J.-M. Li, Y.-P. Li, J.-O. Wang, R. Wu, H.-J. Qian, H.-Q. Wang, K. Ibrahim, *J. Appl. Phys.* **2016**, *119*, 015302.
- [55] X. Wu, Y. Shao, H. Liu, Z. Feng, Y.-L. Wang, J.-T. Sun, C. Liu, J.-O. Wang, Z.-L. Liu, S.-Y. Zhu, Y.-Q. Wang, S.-X. Du, Y.-G. Shi, K. Ibrahim, H.-J. Gao, *Adv. Mater.* **2017**, *29*, 1605407.
- [56] M. Fortin-Deschênes, O. Waller, T. O. Menteş, A. Locatelli, S. Mukherjee, F. Genuzio, P. L. Levesque, A. Hébert, R. Martel, O. Moutanabbir, *Nano Lett.* **2017**, *17*, 4970.
- [57] J. P. Ji, X. F. Song, J. Z. Liu, Z. Yan, C. X. Huo, S. L. Zhang, M. Su, L. Liao, W. H. Wang, Z. H. Ni, Y. F. Hao, H. B. Zeng, *Nat. Commun.* **2016**, *7*, 13352.
- [58] a) A. Castellanos-Gomez, M. Wojtaszek, N. Tombros, N. Agrait, B. J. van Wees, G. Rubio-Bollinger, *Small* **2011**, *7*, 2491; b) C. Lee, H. Yan, L. E. Brus, T. F. Heinz, J. Hone, S. Ryu, *ACS Nano* **2010**, *4*, 2695; c) H. Li, Q. Zhang, C. C. R. Yap, B. K. Tay, T. H. T. Edwin, A. Olivier, D. Baillargeat, *Adv. Funct. Mater.* **2012**, *22*, 1385.
- [59] L. Lu, X. Tang, R. Cao, L. Wu, Z. Li, G. Jing, B. Dong, S. Lu, Y. Li, Y. Xiang, J. Li, D. Fan, H. Zhang, *Adv. Opt. Mater.* **2017**, 1700301.
- [60] W. Tao, X. Ji, X. Xu, M. Ariful Islam, Z. Li, S. Chen, P. E. Saw, H. Zhang, Z. Bharwani, Z. Guo, J. Shi, O. Farokhzad, *Angew. Chem. Int. Ed.*,
DOI:10.1002/ange.201703657.
- [61] a) S. Eigler, A. Hirsch, *Angew. Chem. Int. Ed.* **2014**, *53*, 7720; b) C. R. Ryder, J. D. Wood, S. A. Wells, M. C. Hersam, *ACS Nano* **2016**, *10*, 3900.

- [62] G. Abellan, V. Lloret, U. Mundloch, M. Marcia, C. Neiss, A. Goerling, M. Varela, F. Hauke, A. Hirsch, *Angew. Chem. Int. Ed.* **2016**, *55*, 14557.
- [63] G. Abellan, P. Ares, S. Wild, E. Nuin, C. Neiss, D. Rodriguez-San Miguel, P. Segovia, E. G. Michel, A. Görling, F. Hauke, J. Gomez-Herrero, A. Hirsch, F. Zamora, *Manuscript submitted for publication*.
- [64] S. Zhang, W. Zhou, Y. Ma, J. Ji, B. Cai, S. A. Yang, Z. Zhu, Z. Chen, H. Zeng, *Nano Lett.*, DOI: 10.1021/acs.nanolett.7b00297.

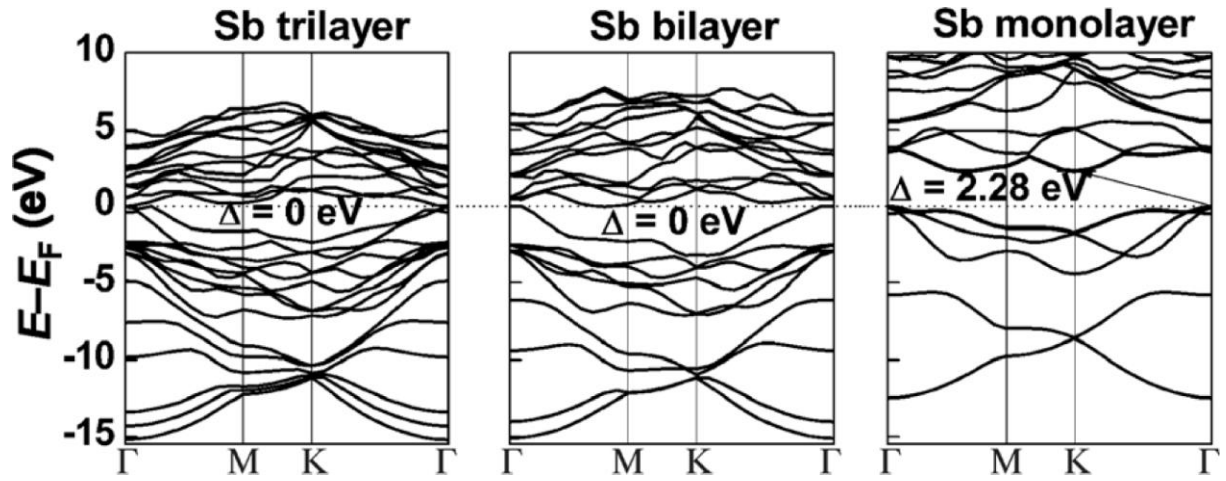


Figure 1. Electronic band structures of Sb trilayers, bilayers, and monolayers calculated at the HSE06 DFT functional. Dots: Fermi levels. Reproduced with permission.^[12a]

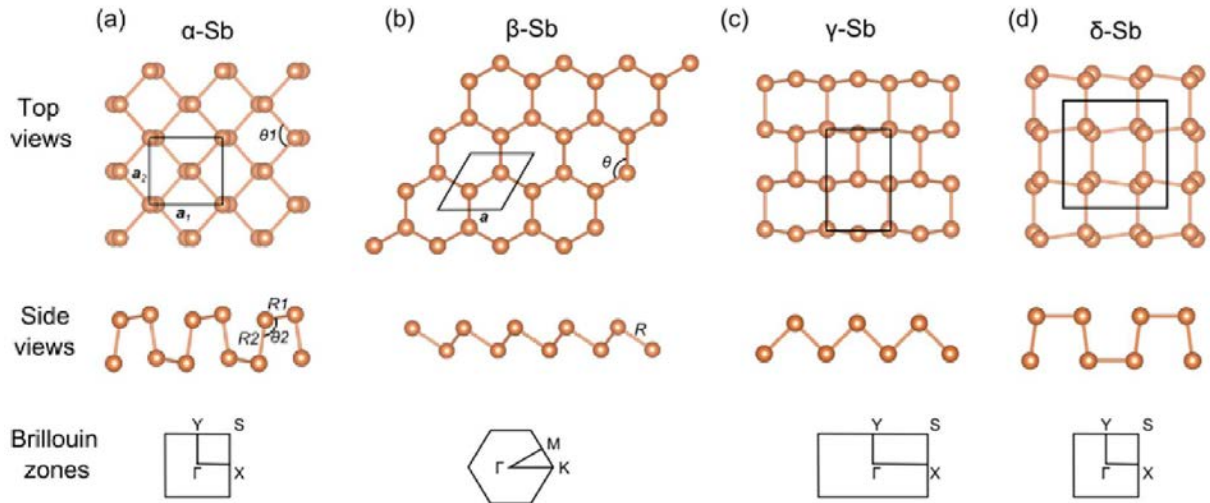


Figure 2. Different structural phases of antimonene allotropes: a) α -, b) β -, c) γ -, and d) δ -antimonene. Reproduced with permission.^[13]

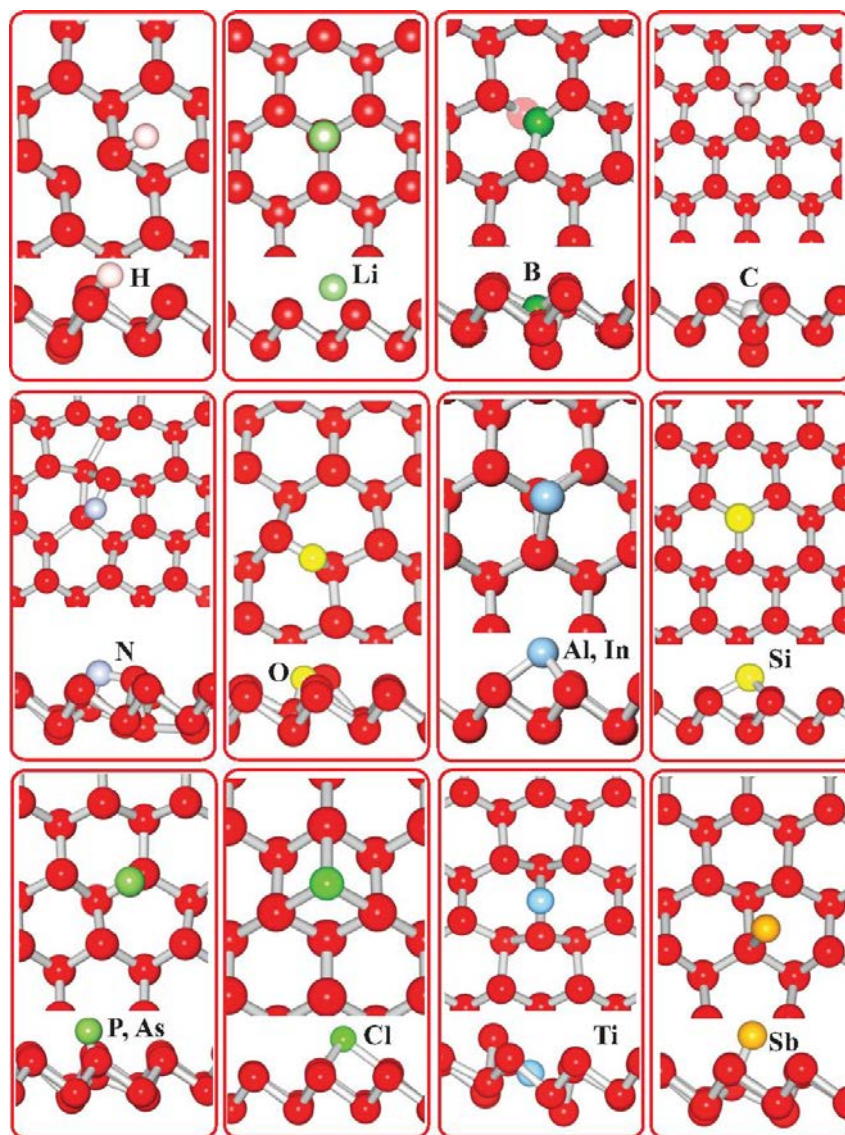


Figure 3. Top and side views of optimized atomic structure of β -antimonene after the adsorption of different adatoms. Sb atoms are shown by red balls and adsorbed adatoms are presented by balls with different colors(also adsorbed SB). Reproduced with permission.^[17a]

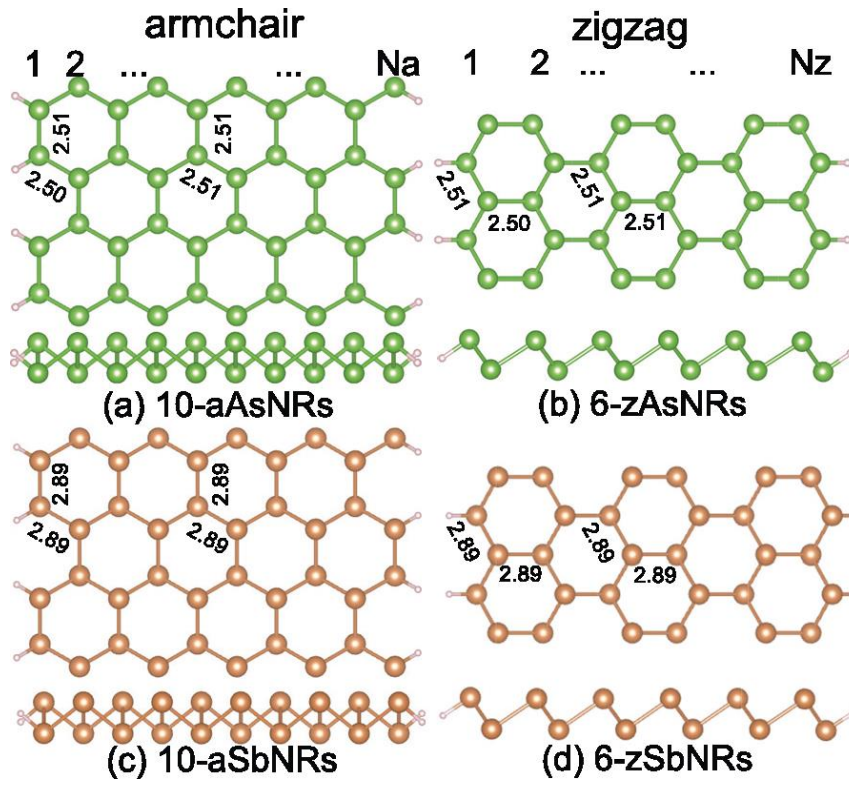


Figure 4. Top and lateral views of armchair and *zig-zag* nanoribbons of a), b) arsenene and c), d) antimonene. N_a (N_z) denotes the number of dimer lines (*zig-zag* chains) across the nanoribbon width. Bond lengths are also indicated. Reproduced with permission.^[19]

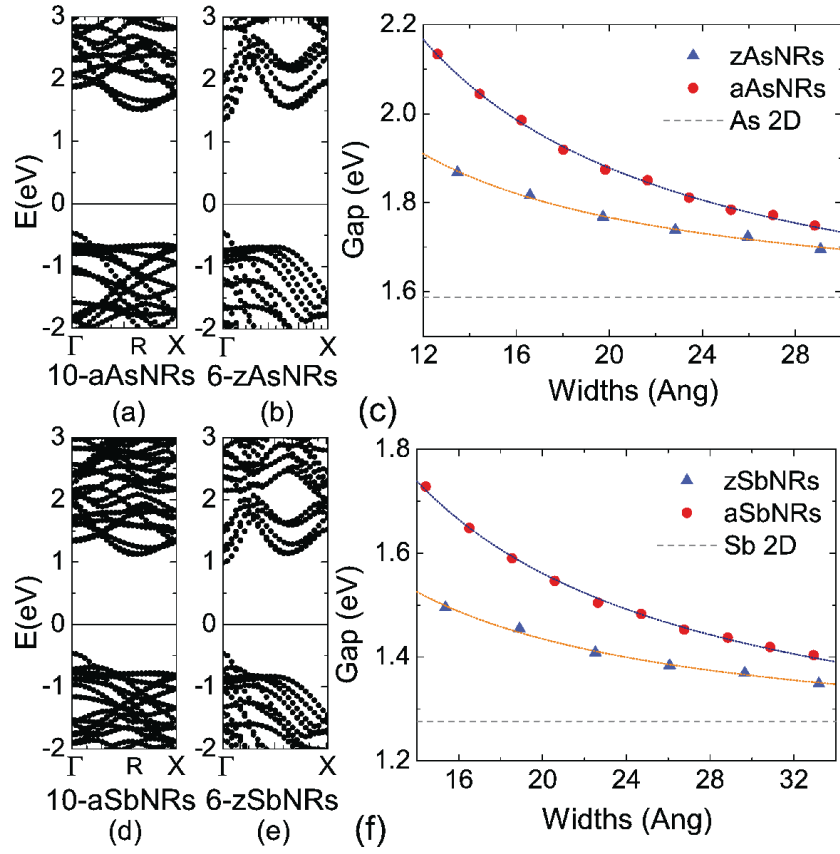


Figure 5. Band structures of a) 10-aAsNRs, b) 6-zAsNRs, d) 10-aSbNRs, and e) 6-zSbNRs, where the Fermi level has been set to 0 eV. Band gap variations as a function of ribbon widths for c) arsenene and f) antimonene nanoribbons. The dot lines correspond to a fit. Reproduced with permission.^[19]

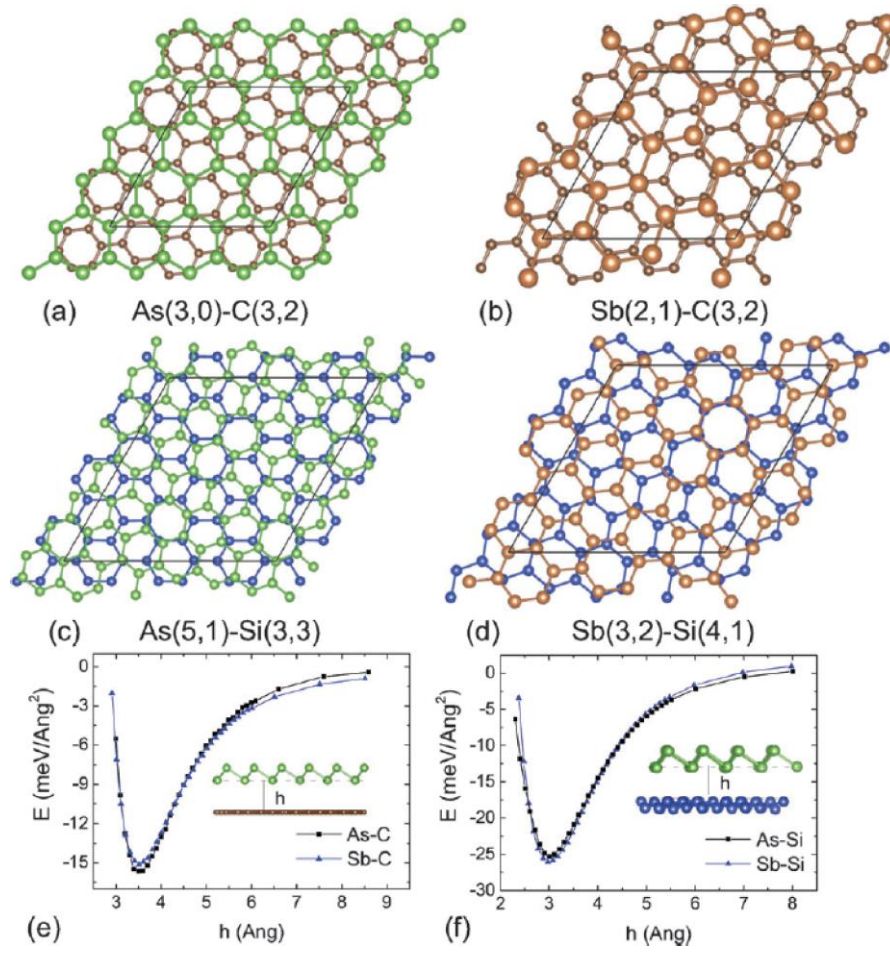


Figure 6. The structures of a) arsenene-graphene, b) antimonene-graphene, c) arsenene-silicene, and d) antimonene-silicene hetero-bilayers. The binding energies as a function of interlayer distances for the e) arsenene/antimonene-graphene and f) arsenene/antimonene-silicene ones. Reproduced with permission.^[23]

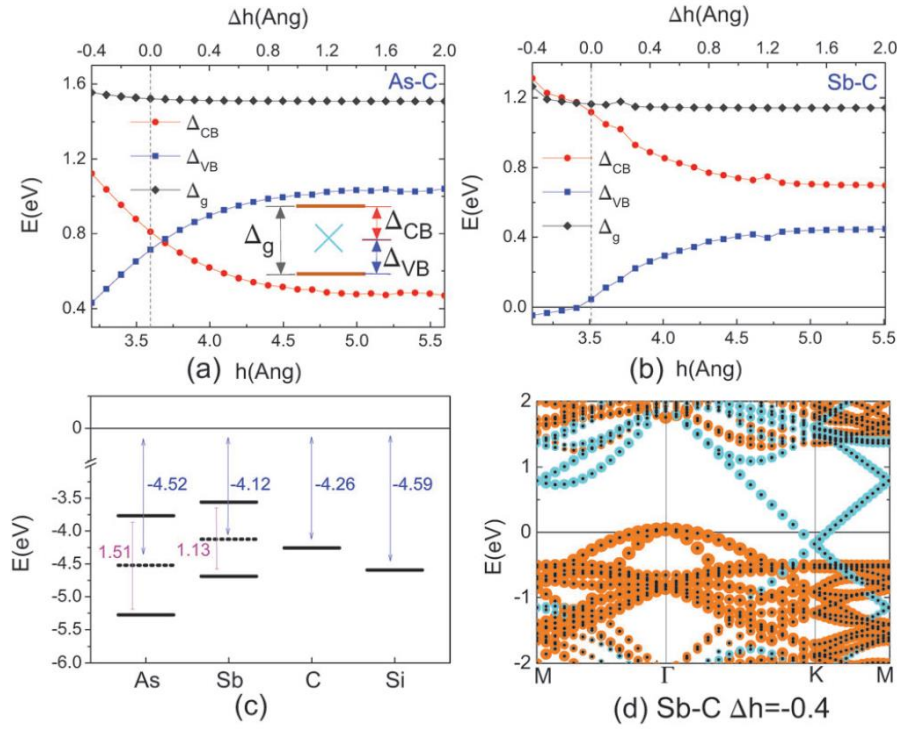


Figure 7. Schottky barrier evolution for a) arsenene-graphene and b) antimonene-graphene bilayers. c) Band alignment of band edges for isolated arsenene, antimonene, graphene, and silicene monolayers where the zero is the vacuum level. d) Band structure of the antimonene-graphene bilayer under a compression strain of $\Delta h = -0.4$ Å. The bands projected onto Sb and C orbitals are highlighted by orange and cyan circles, and the size corresponds to the weight of each species. Reproduced with permission.^[23]

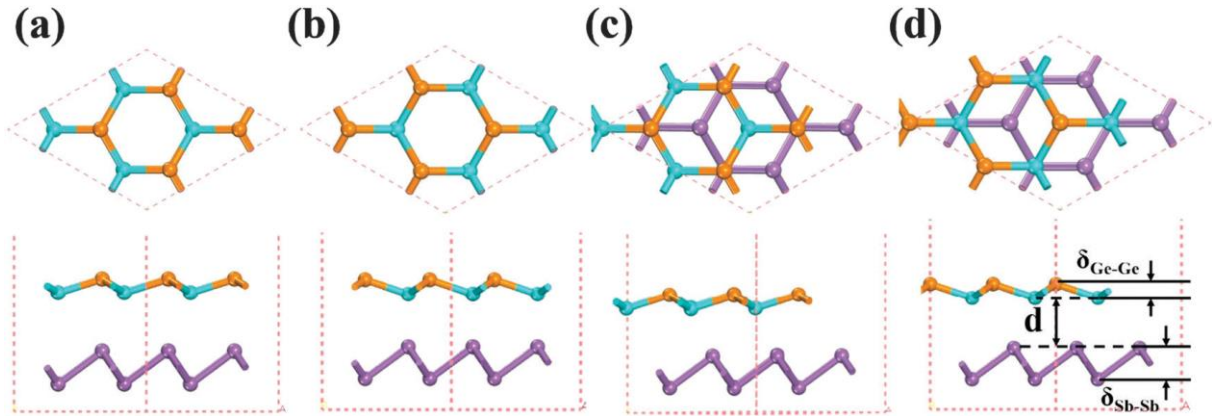


Figure 8. Top and side views of a germanene-antimonene bilayer for different patterns: a) pattern AAI, b) pattern AAIL, c) pattern ABI, d) pattern ABII. The d in pattern ABII denotes the interlayer distance. $\delta_{\text{Ge-Ge}}$ and $\delta_{\text{Sb-Sb}}$ represent the buckling heights of the germanene and antimonene layers, respectively. The Sb atoms of antimonene and the Ge atoms at the upper and lower levels are represented by purple, yellow and blue balls, respectively. Red dashed lines represent the unit cells. Reproduced with permission.^[24]

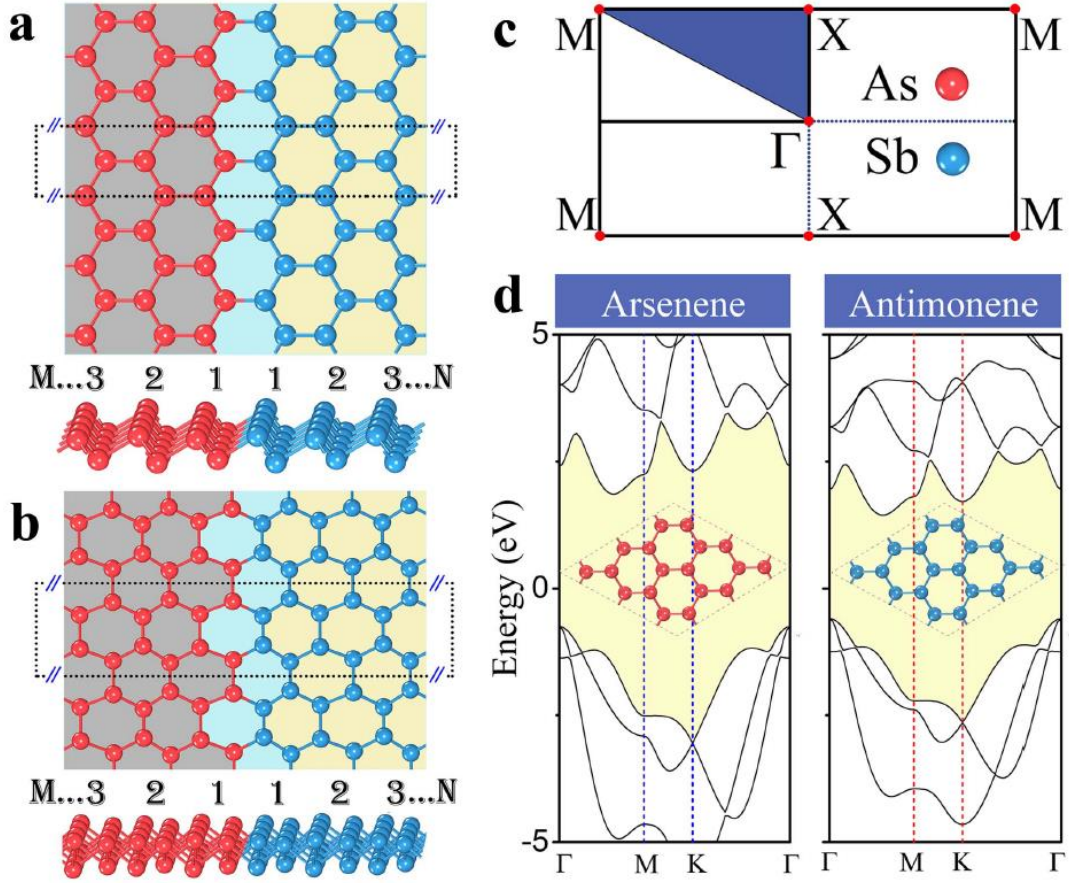


Figure 9. Atomic configurations of arsenene-antimonene lateral heterostructures a) with zigzag interlines, and b) with armchair interlines from the top and side views. The dashed rectangle denotes the unit cell of the systems. c) The 2D Brillouin zone of the monolayers with high symmetry points. d) Band structures of the pristine arsenene and antimonene. Reproduced with permission.^[25]

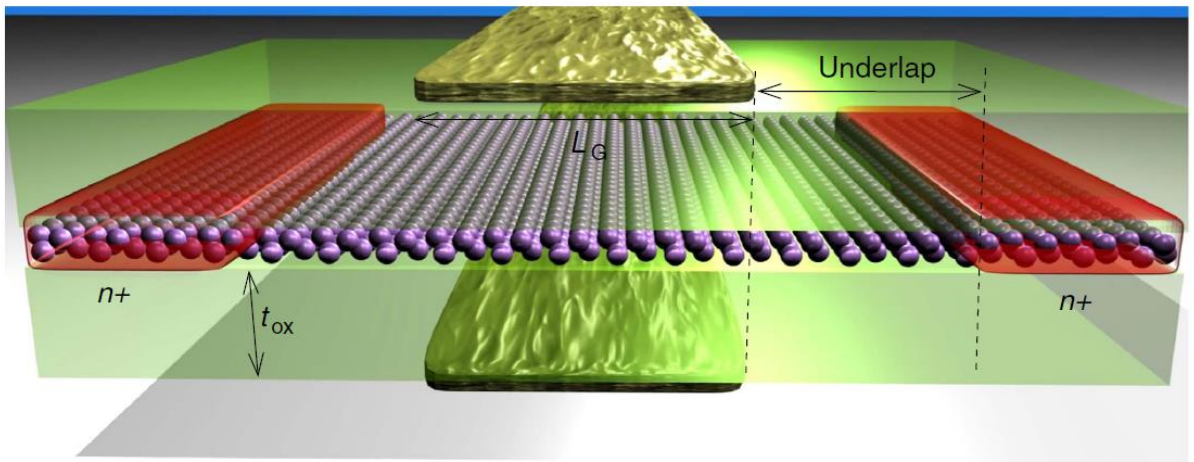


Figure 10. Pictorial representation of a double-gate n-doped MOSFET studied in Reference^[26], where the middle channel is either made of arsenene or antimonene. In the figure, the doped contacts, the gate and the oxide are also shown, along with the main geometrical parameters of the device. Reproduced with permission.^[26]

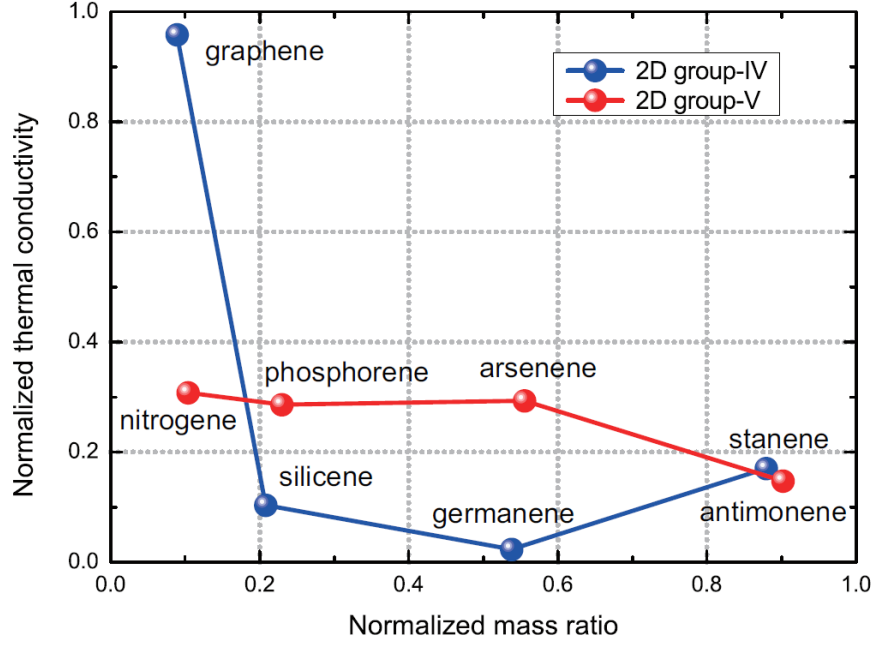


Figure 11. Normalized thermal conductivities of elemental 2D materials at 300 K. Reproduced with permission.^[27]

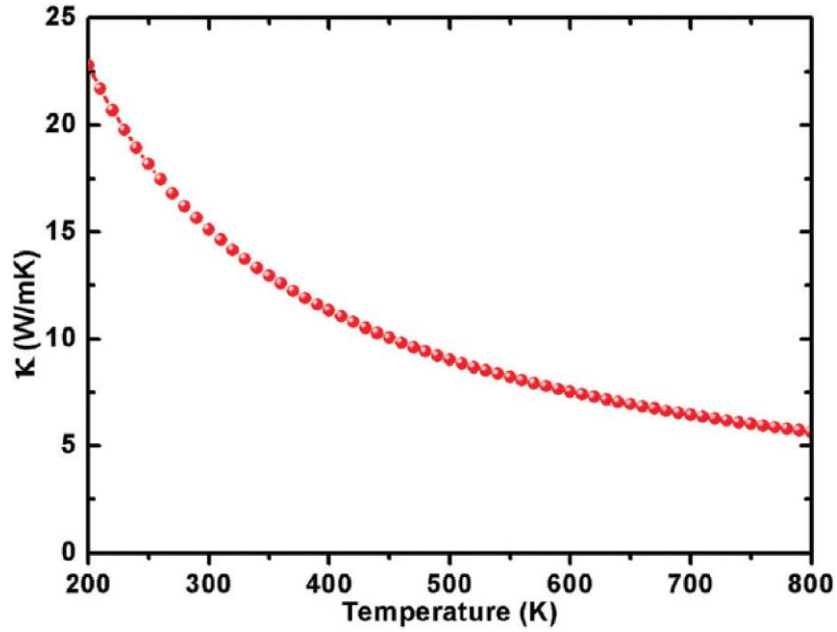


Figure 12. The lattice thermal conductivity of antimonene as a function of temperature. Reproduced with permission.^[28]

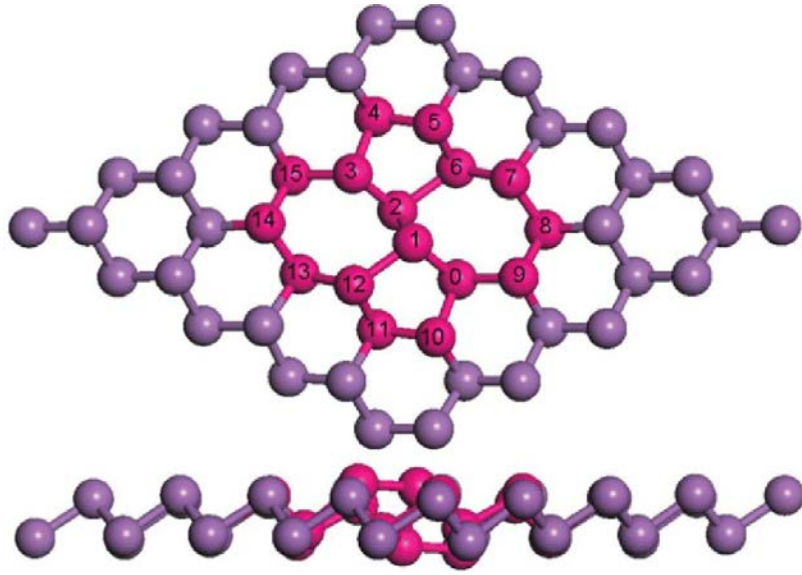


Figure 13. The top and side views of the fully relaxed antimonene with a Stone-Wales defect. All the spheres represent Sb atoms and the pink spheres represent the most related Sb atoms to SW defect. Reproduced with permission.^[31]

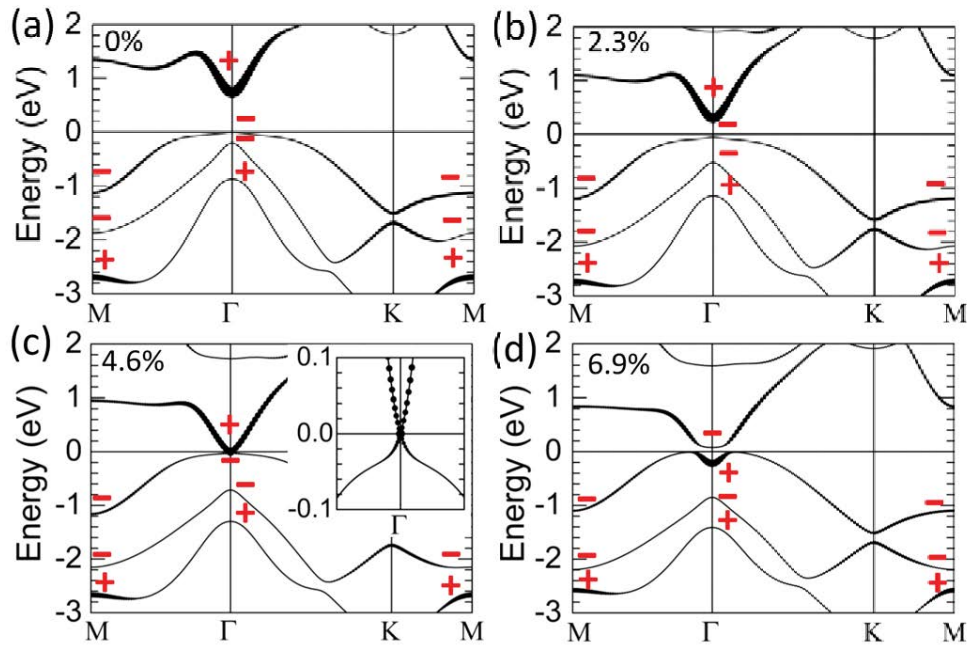


Figure 14. Band structure of antimonene under a) 0%, b) 2.3%, c) 4.6%, and d) 6.9% strain. The inset in (c) is a zoom near the Γ point. The path in Brillouin zones is M- Γ -K-M. The size of the black circles is proportional to the contribution on the s-type orbital. Reproduced with permission.^[21]

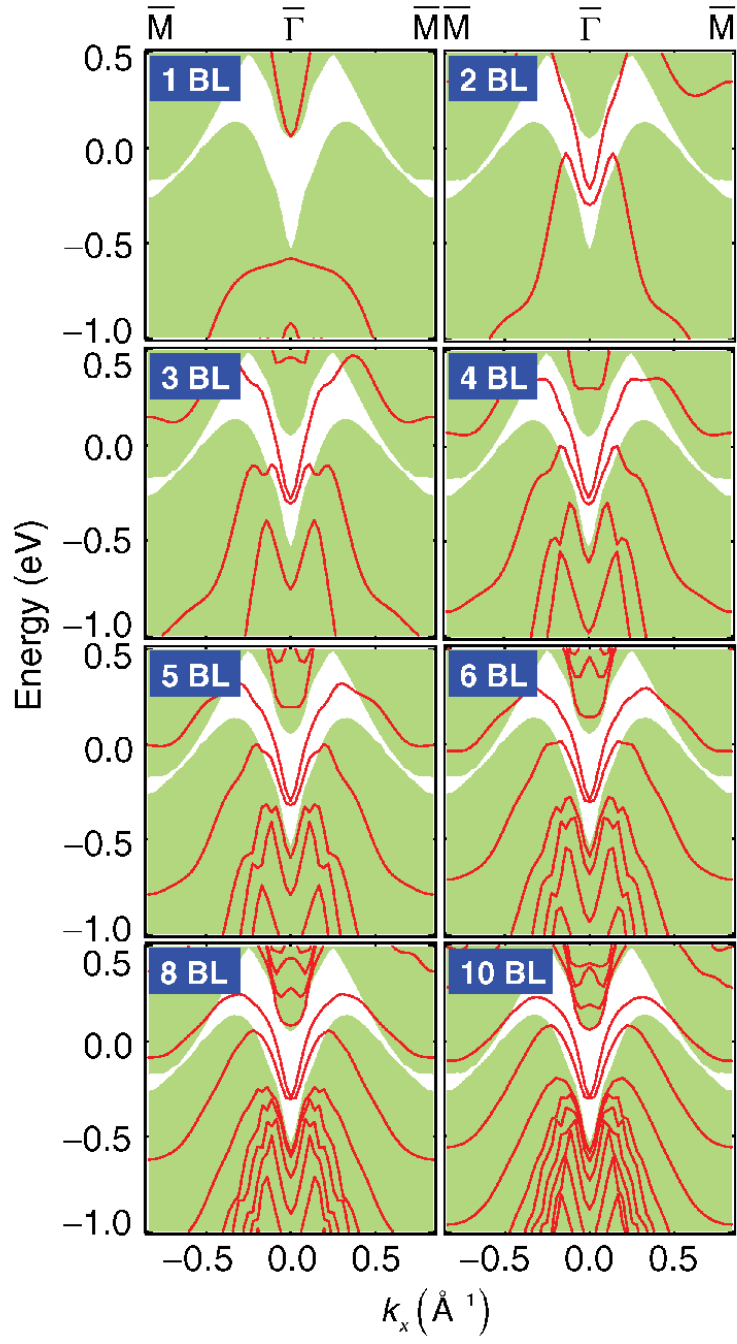


Figure 15. Band structure of Sb(111) films of various thicknesses. The shaded areas indicate projected bulk band regions. Reproduced with permission.^[11a]

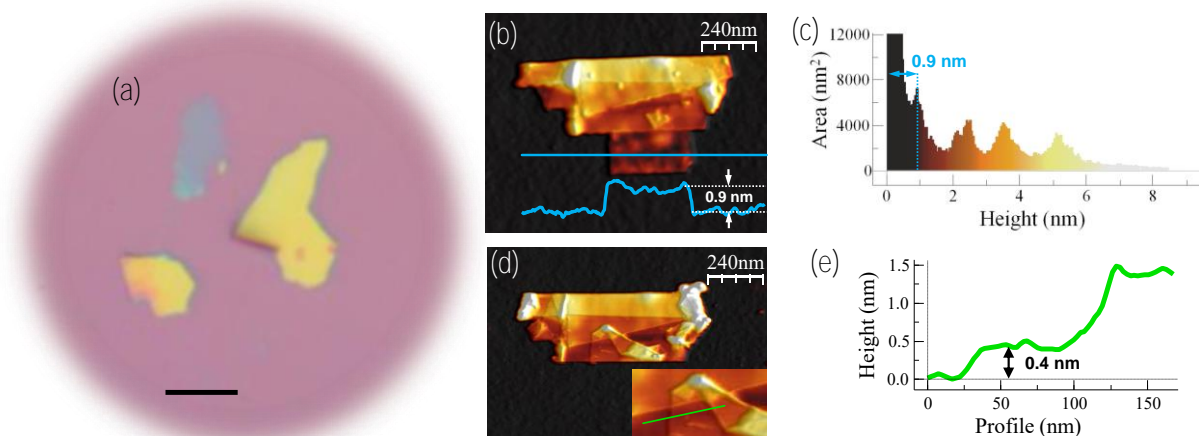


Figure 16. a) Optical micrograph showing up to three large flakes of antimony. Black scale bar 10 μm . Different colors correspond to different thicknesses. b) AFM topographic image where an $\sim 0.2 \mu\text{m}^2$ antimonene flake with terraces of different heights can be seen. The profile on the bottom corresponds to the blue horizontal line in the image. c) Height histogram of the image in (b) showing the different thicknesses of the terraces. The substrate peak has been cut to 12000 nm^2 for the sake of clarity. The minimum step height is $\sim 0.9 \text{ nm}$ compatible with an antimonene monolayer adsorbed in the presence of water. d) Same flake as in (b) but after a nanomanipulation process. The lowest terrace was folded upward resulting in a structure with different folds. The inset shows the area of the folded structure where the lowest step height is found. e) Profile corresponding to the green line in the inset in (d). The lowest step height is $\sim 0.4 \text{ nm}$ corresponding to an antimonene monolayer. Reproduced with permission.^[18]

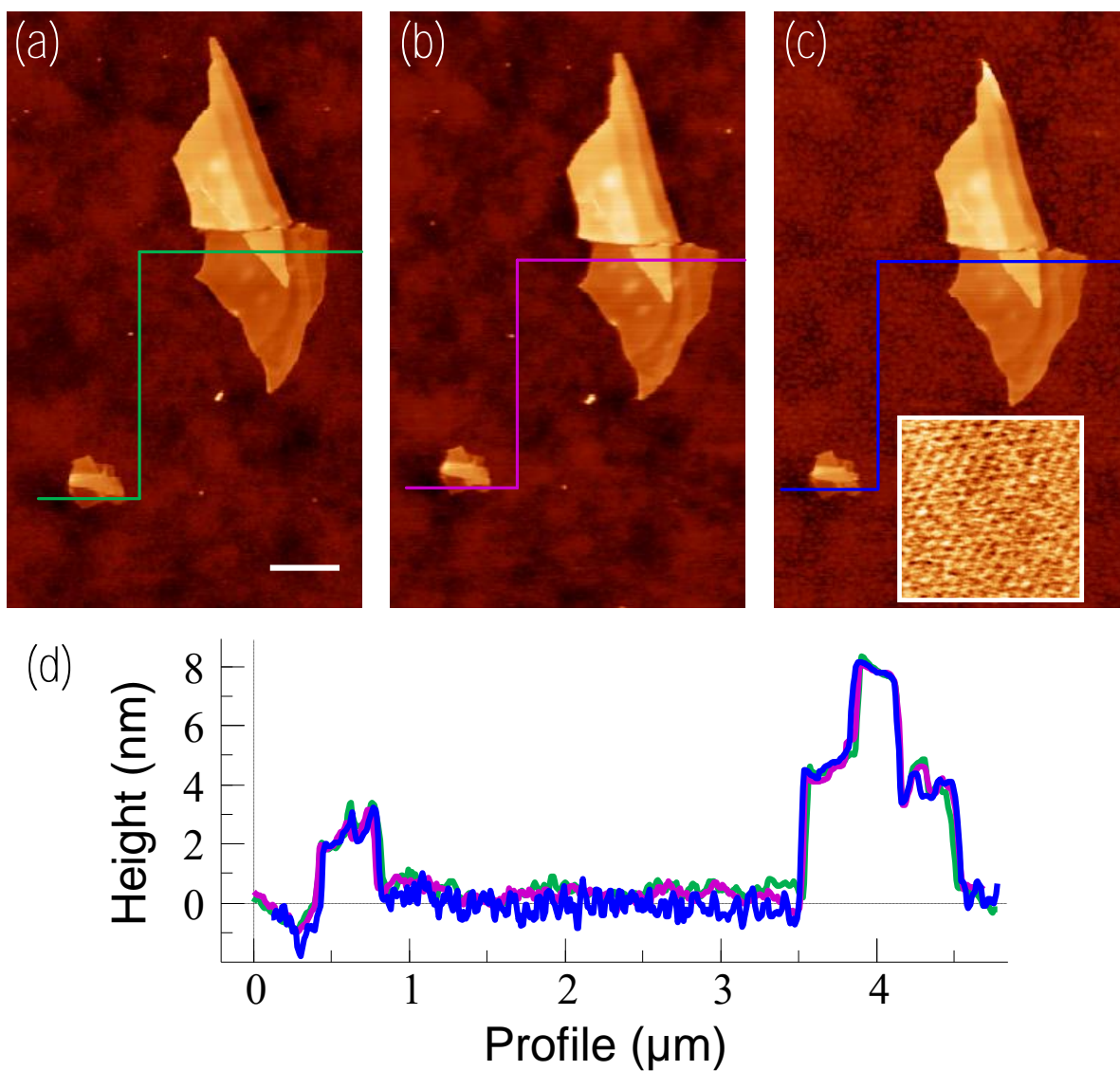


Figure 17. a) Image of two antimonene sheets acquired just after exfoliation. White scale bar 500 nm. b) Same as in (a) but two months later. c) Image acquired immediately after (b) but in this case the sample was immersed in water. The inset reveals atomic periodicity compatible with the atomic lattice of antimonene. d) Profiles along the lines in (a-c). Reproduced with permission.^[18]

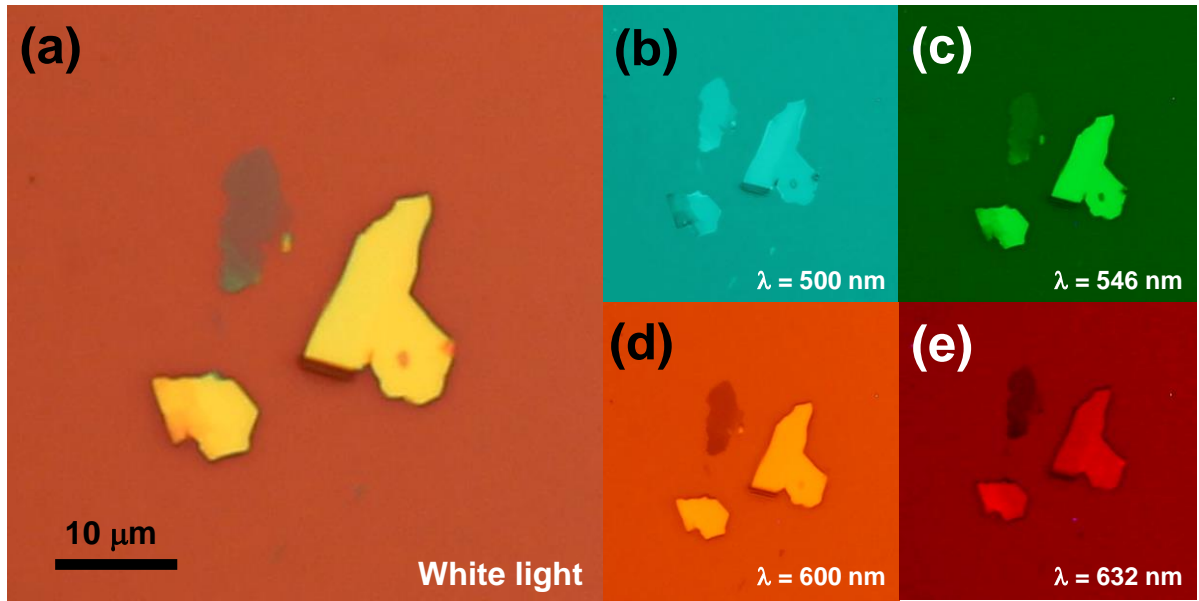


Figure 18. Different optical images acquired using a) white light and (b–e) narrow-bandpass filters (500, 546, 600, and 632 nm, respectively). Reproduced with permission.^[45]

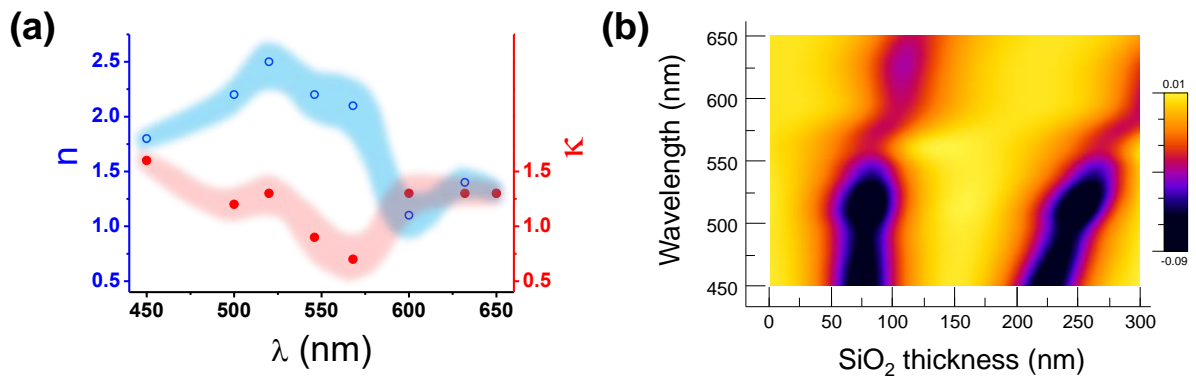


Figure 19. a) Refractive index (blue open circles, left axis) and extinction coefficient (red solid circles, right axis) of few-layer antimonene determined as functions of the incident wavelength. b) Optical contrast as a function of SiO₂ layer thickness and incident light wavelength for antimonene. Reproduced with permission.^[45]

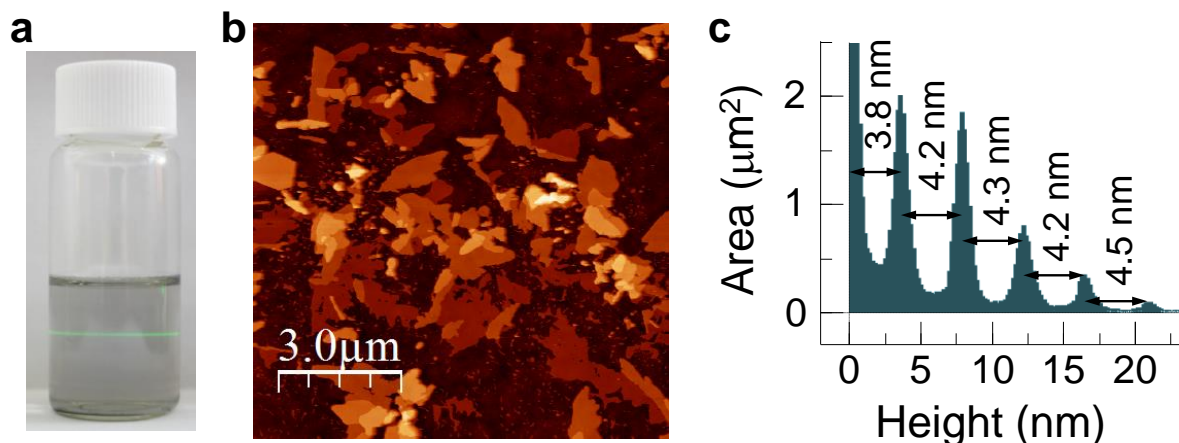


Figure 20. a) Photograph of a dispersion of exfoliated few-layer antimonene where Faraday-Tyndall effect can be observed. b) Topographic AFM image of few-layer antimonene on a SiO₂/Si substrate deposited by drop casting showing over micron lateral dimensions. c) Height histogram of the image in (b) showing the different thicknesses of the terraces. The substrate peak has been cut to 2.5 μm² for the sake of clarity. A minimum constant thickness of ~ 4 nm can be easily observed. Reproduced with permission.^[48]

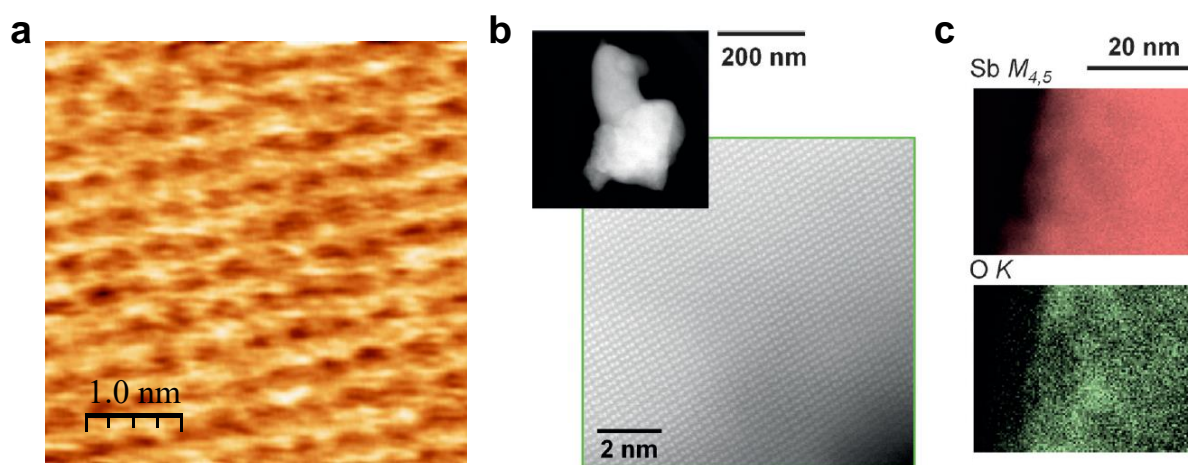


Figure 21. a) AFM showing atomic periodicity. b) Low magnification high angle annular dark field (HAADF) image of a flake (top left) together with an atomically-resolved image (acquired along the [0 -1 2] direction). c) Two-dimensional EELS maps taken near the flake edge, where the signals below the Sb M_{4,5} (red) and O K (green) absorption edges can be seen. Reproduced with permission.^[48]

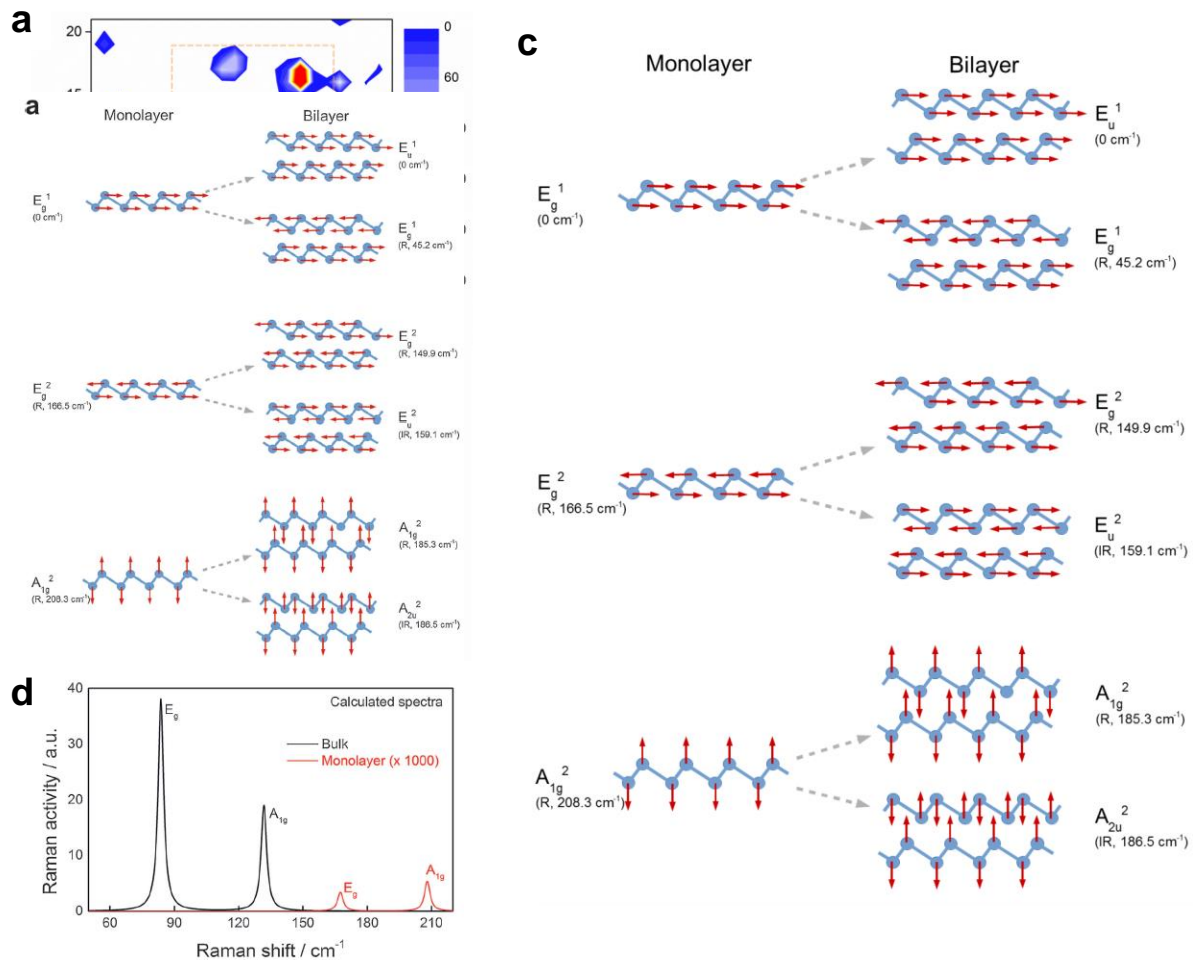


Figure 22. a) A_{1g} intensity Raman map of liquid phase exfoliated antimonene drop-casted on a SiO_2/Si substrate, depicting the presence of several flakes. b) Single-point spectra at different thicknesses in accordance with topographic AFM imaging (inset) of the same area as in (a). The dashed square marks the position of the AFM image shown in (b). c) Atomic displacement patterns for the G point phonon modes in single layer antimonene (left) and in the bilayer material (right). The E_g and E_u modes are doubly degenerate, and each mode has a partner mode (not shown) of the same frequency, where atoms vibrate perpendicularly to the plane of the paper. The out-of-plane acoustic A_{2u}^1 mode in single layer antimonene is the origin of two additional modes in the bilayer structure, the acoustic A_{2u}^1 and the optical A_{1g}^1 mode (both not shown). The calculated frequencies and infrared (IR) or Raman (R) activity are indicated in parentheses. d) Calculated Raman spectra for bulk Sb and monolayer antimonene. The very low intensity of the Raman signals for a monolayer (> 1000 times less Raman active than for the bulk case), precludes its detection, as observed experimentally. Reproduced with permission.^[48]

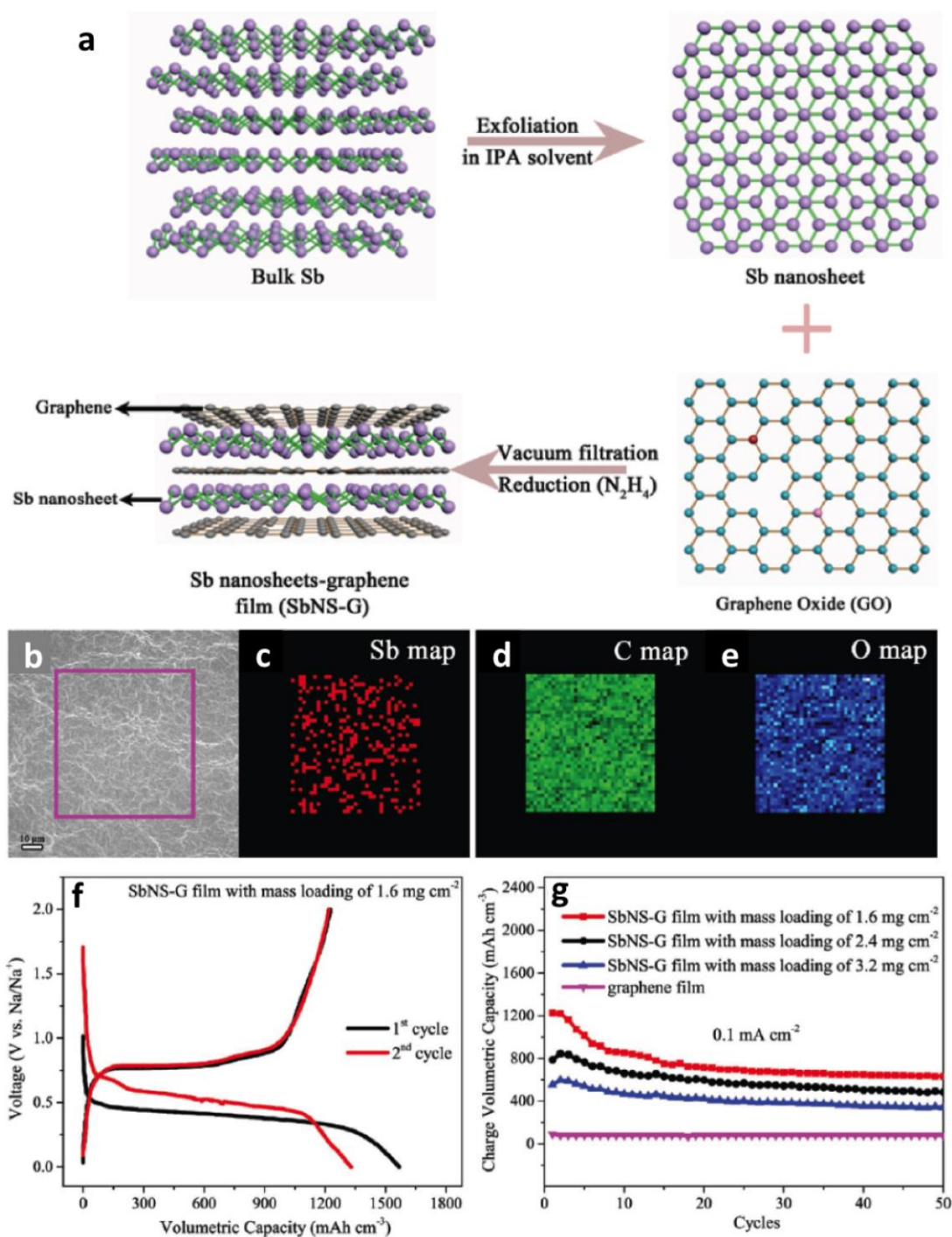


Figure 23. a) Schematic representation of the fabrication process of Sb nanosheets-Graphene (SbNS-G) film. Bulk Sb powders were first exfoliated in an isopropanol solution to obtain ultrathin Sb nanosheets; subsequently, the as-prepared Sb nanosheets were mixed with graphene (Sb:GO = 4:1) and then collected to by vacuum filtration and chemically reduced to an uniform SbNS-G film. b) Typical scanning electron microscopy image of SbNS-G film, which shows the uniform property and corresponding elemental mapping images of c) antimony, d) carbon, and e) oxygen in the pink rectangular frame area in (b), which reflects the uniformly distribution of Sb, C, and O in the film. f) Selected first-two charge–discharge curves of SbNS-G film (1.6 mg cm^{-2}) at a current density of 0.1 mA cm^{-2} . g) Cyclic performances of SbNS-G and graphene films at a current density of 0.1 mA cm^{-2} , respectively. Reproduced with permission.^[52]

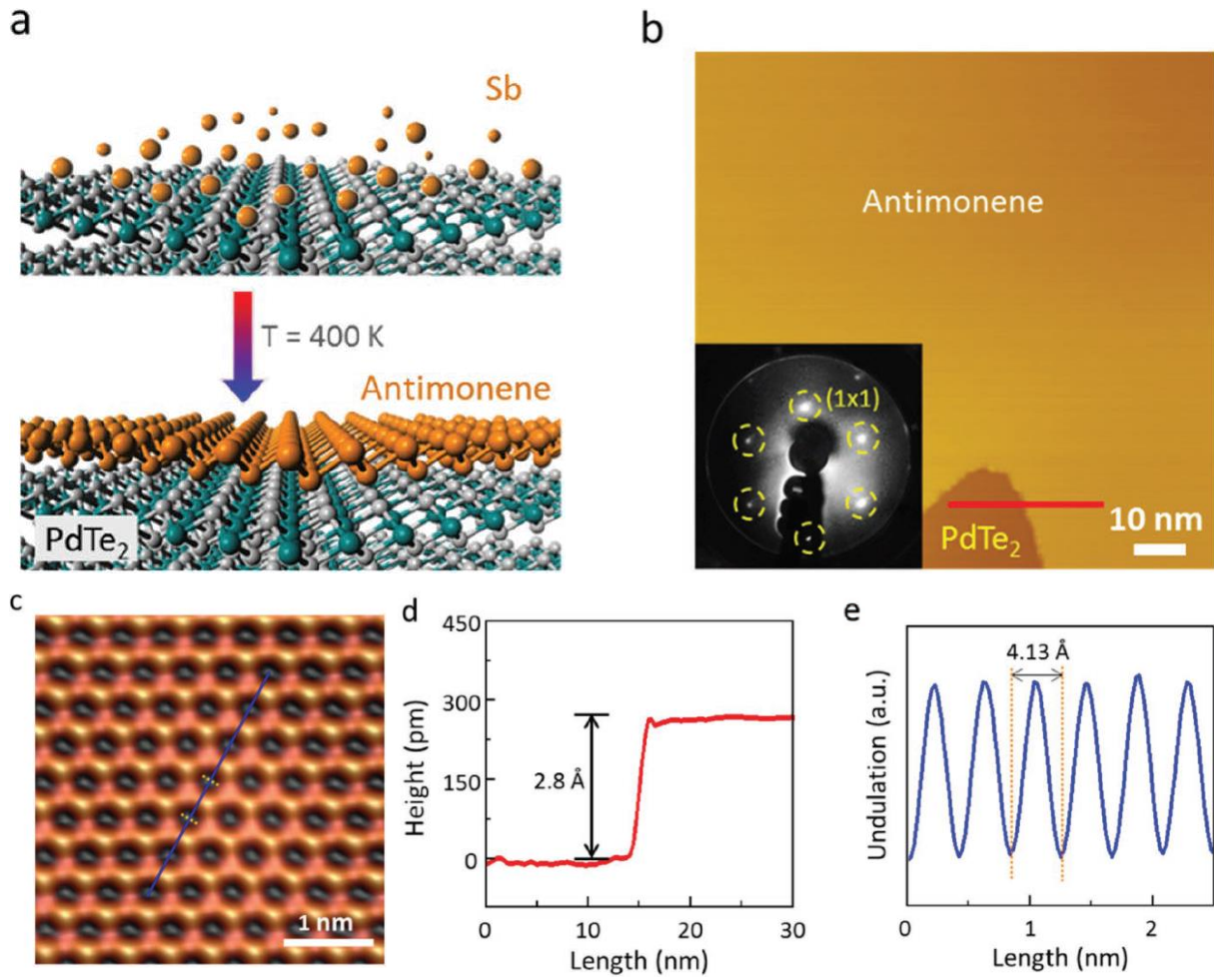


Figure 24. a) Schematic of fabrication. b) STM topographic image (-2.0 V , -10 pA) of large antimonene island on PdTe₂. Inset: LEED pattern of antimonene on PdTe₂. The six diffraction spots are due to the antimonene (1x1) structure with respect to the substrate. c) Atomic resolution STM image (-1.5 V , -200 pA) of monolayer antimonene with enhanced visibility showing the graphene-like honeycomb. d) Height profile corresponding to the red line in (b), showing that the antimonene island presents an apparent height of 2.8 Å . e) Line profile corresponding to the blue line in (c), revealing the periodicity of the antimonene lattice ($4.13 \pm 0.02\text{ Å}$). Reproduced with permission.^[55]

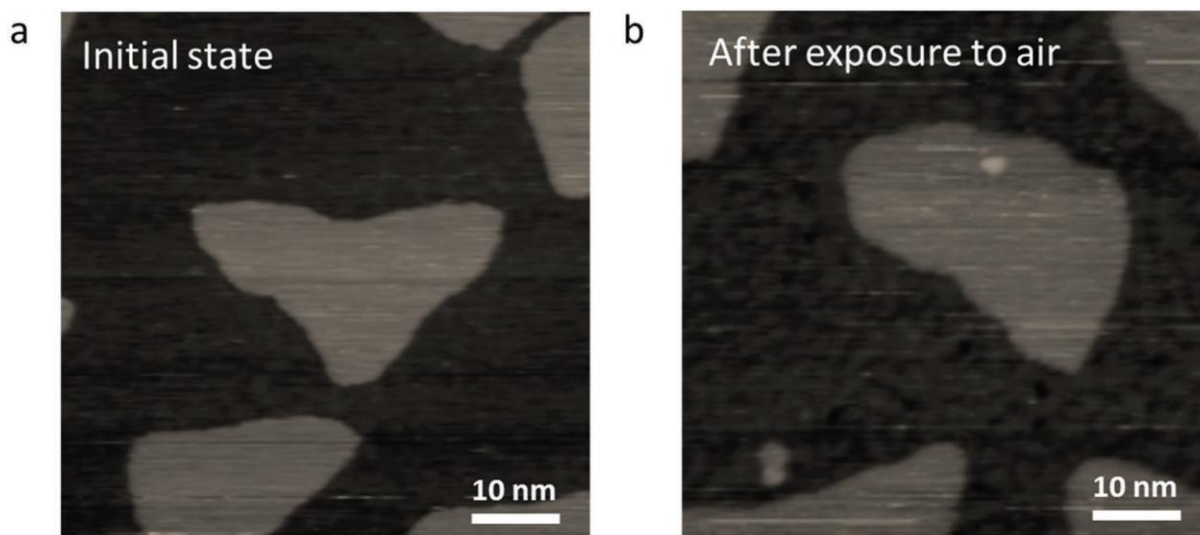


Figure 25. a) Typical STM image (-2.0 V, -100 pA) of antimonene islands on PdTe_2 substrate before air exposure. The surface of the islands is smooth without impurities. b) STM image (-2.0 V, -100 pA) of the same sample after exposing to air for 20 min. Reproduced with permission.^[55]

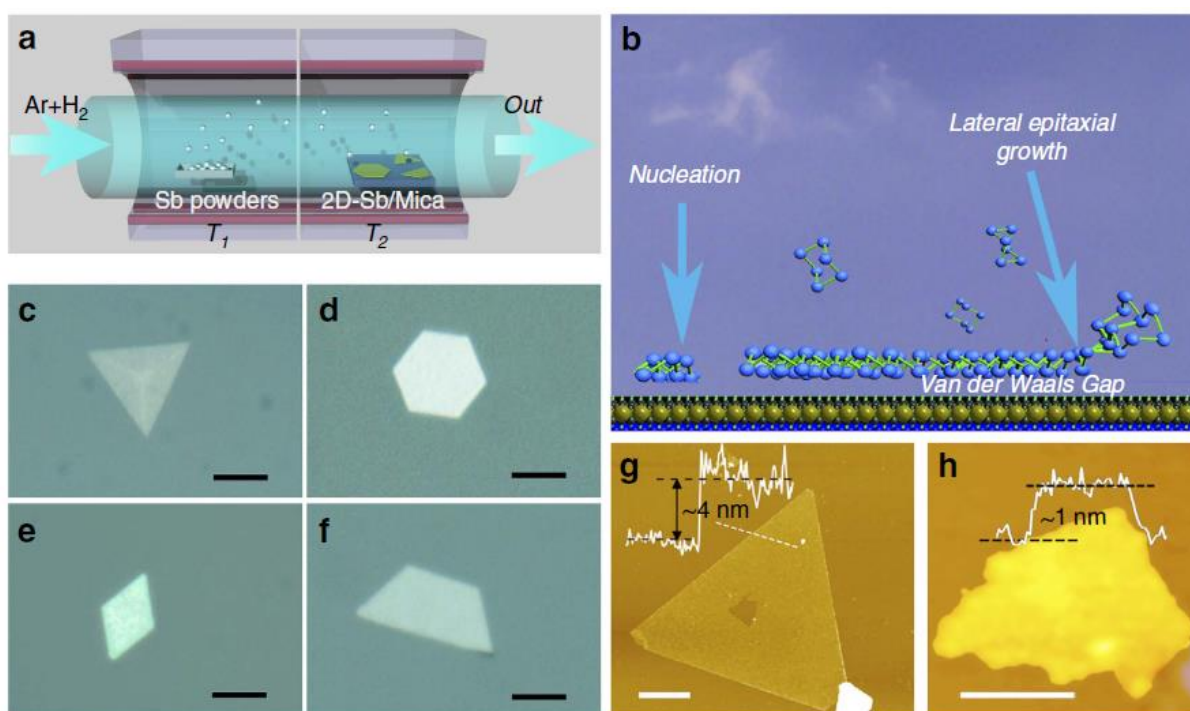


Figure 26. Antimonene polygons synthesized *via* van der Waals epitaxy on mica substrates. a) Schematic illustration of the sample synthesis configurations. b) Schematic diagram of van der Waals epitaxy. c–f) Optical images of typical antimonene polygons with triangular, hexagonal, rhombic and trapezoidal shapes, respectively. The scale bar is $5\ \mu\text{m}$. g) AFM image of a typical triangular antimonene sheet. The thickness is $4\ \text{nm}$. The scale bar is $1\ \mu\text{m}$. h) AFM image of a tiny antimonene sheet. The thickness is $\sim 1\ \text{nm}$. The scale bar is $50\ \text{nm}$. Reproduced with permission.^[57]

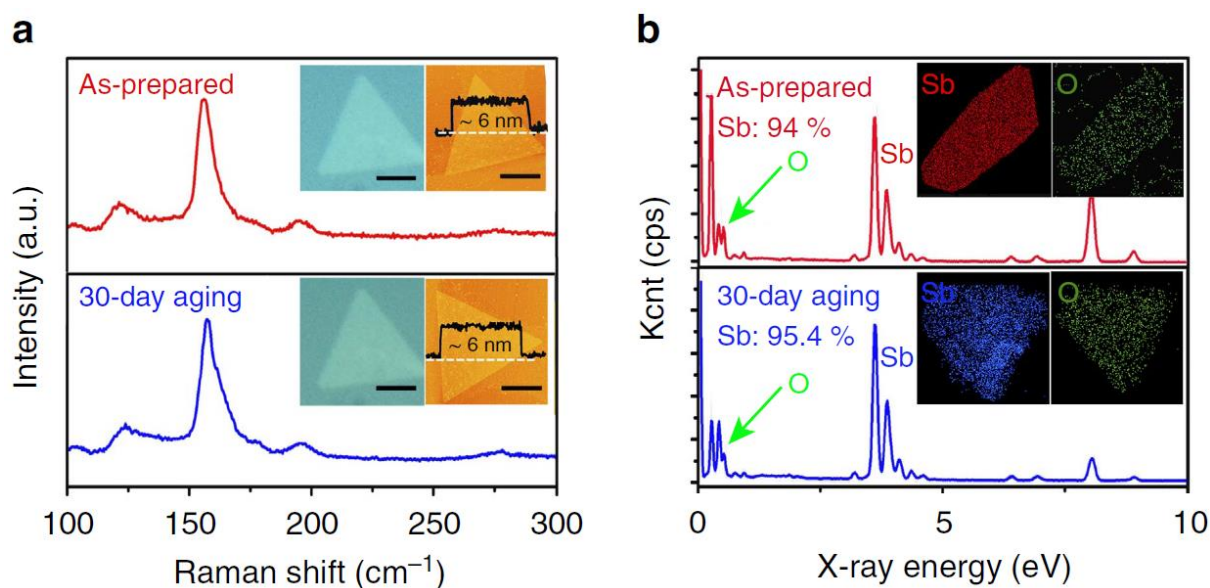


Figure 27. a) Optical images, AFM images and Raman spectra of antimonene layers before and after a 30-day aging. The scale bar is 2 μm . b) EDS analysis of antimonene sheets randomly selected on the copper grid before and after a 30-day aging. Reproduced with permission.^[57]

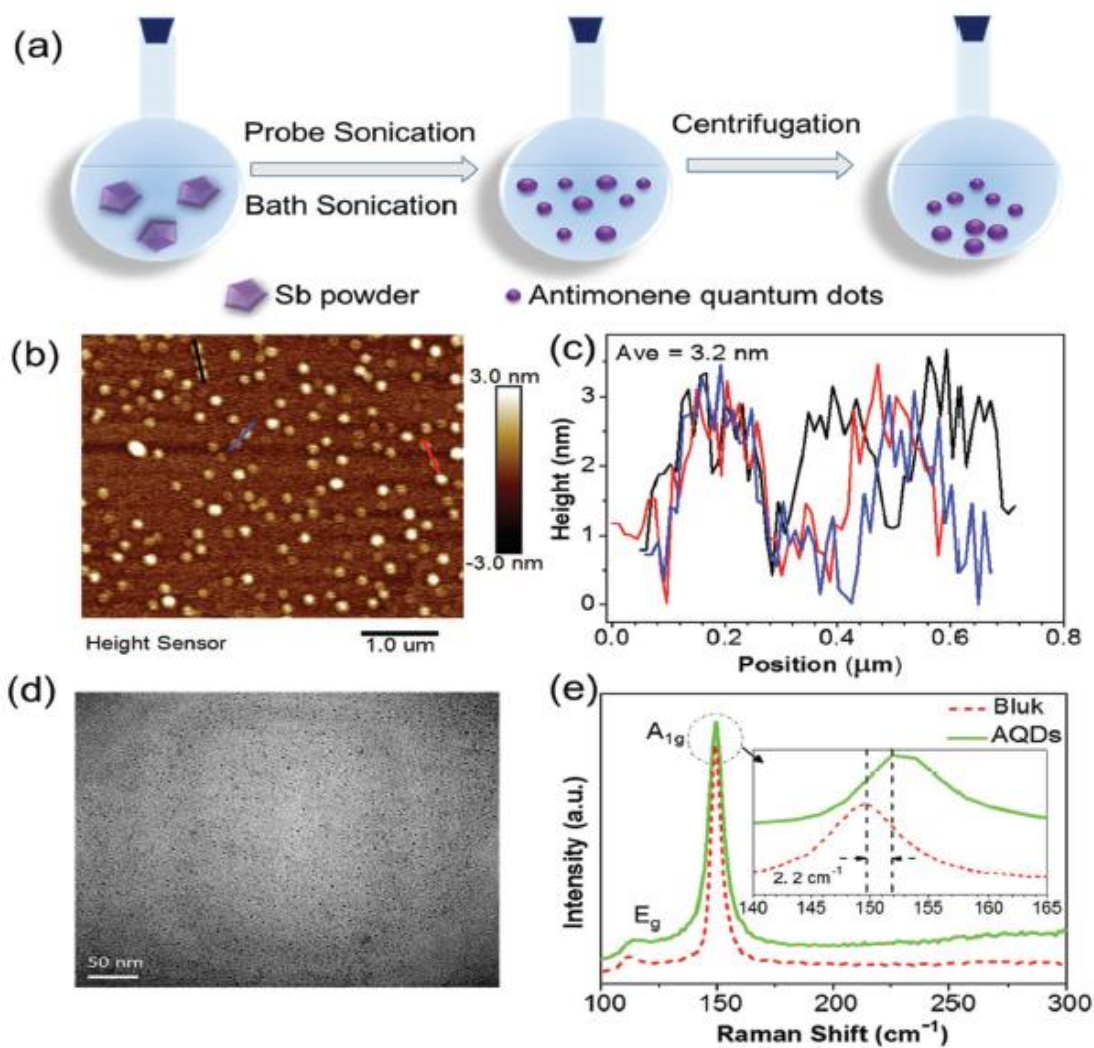


Figure 28. a) Schematic illustration of the antimonene quantum dots synthesis. b) AFM topographic image of AQDs prepared using NMP as a solvent. c) Height profiles along the lines in b). d) TEM image. e) Raman analysis of bulk antimony and AQDs. Reproduced with permission.^[59]

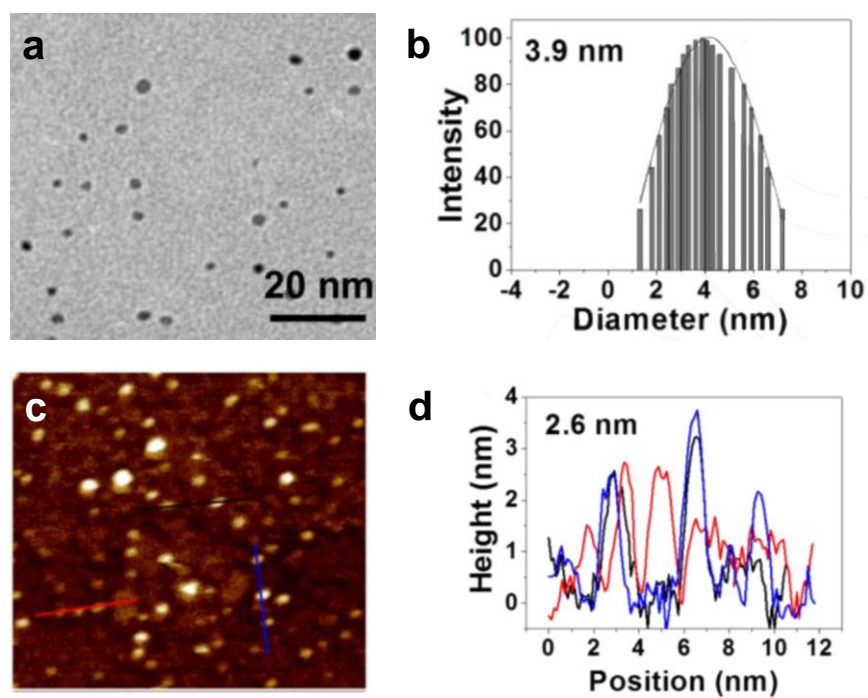


Figure 29. Characterization of AQDs synthesized using ethanol as a solvent. a) TEM image. b) Diameter distribution from TEM data. c) AFM topographic image. d) Height profiles along the lines in c). Reproduced with permission.^[60]

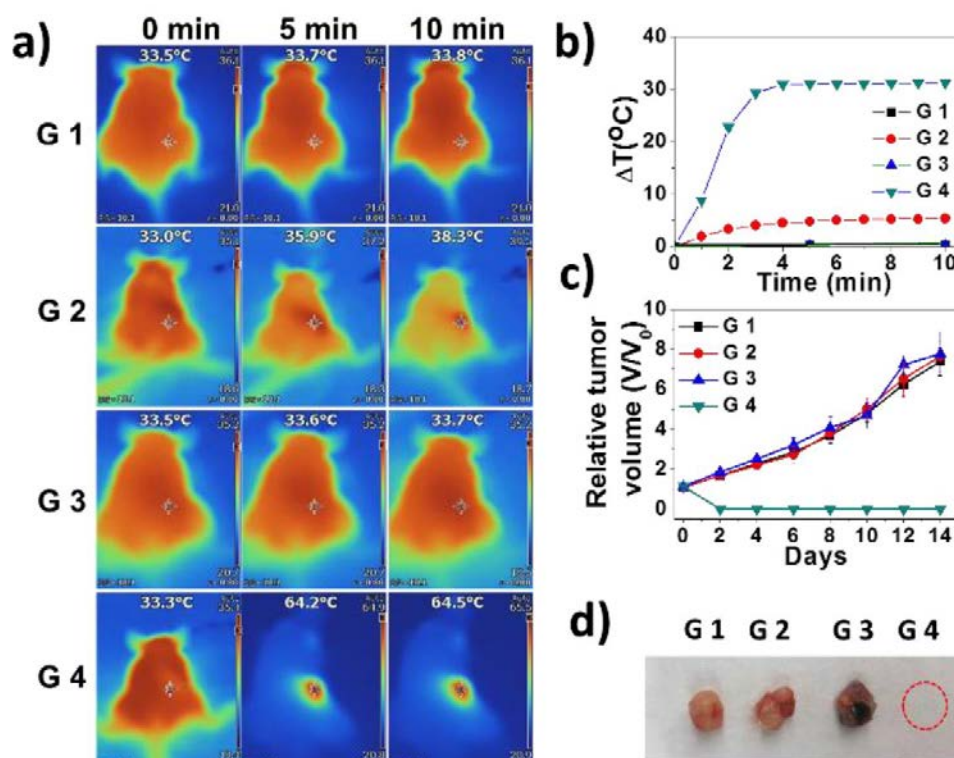


Figure 30. a) Infrared images of MCF-7 tumor-bearing mice under different treatments (G1: Saline; G2: only NIR; G3: only PEG-coated AQDs; G4: PEG-coated AQDs + NIR; 808 nm, 1 Wcm⁻²). b) Temperature changes at tumor sites. c) Relative tumor volumes. d) Representative images of tumors after harvesting at day 14. Reproduced with permission.^[60]

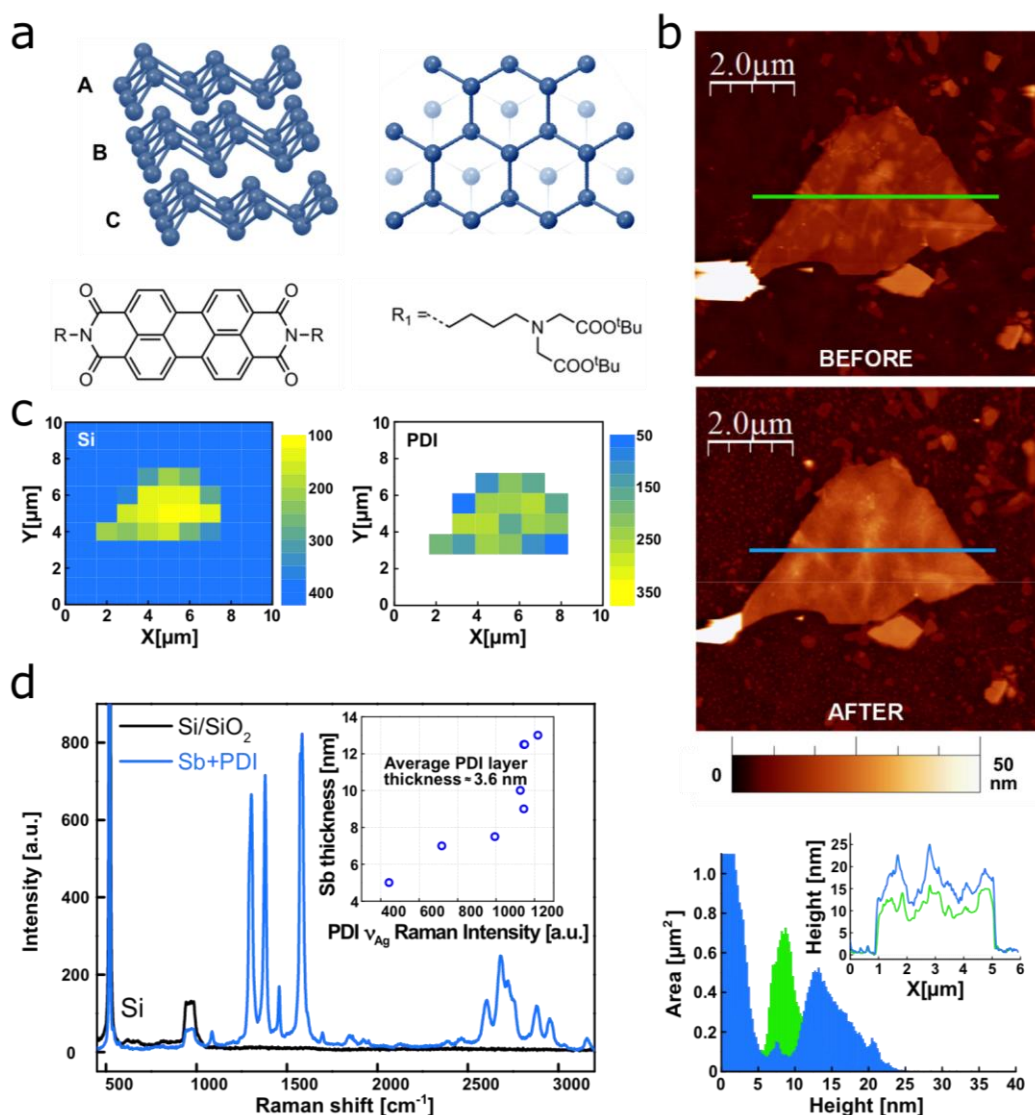


Figure 31. a) Structure of β -antimonene (top panel) and the perylene bisimide (PDI) molecule (bottom panel). b) AFM topographic images showing an antimonene flake of *ca.* 10 nm of thickness. Top: Flake as deposited. Middle: Same flake after the functionalization with PDI molecules. Bottom: Height histograms of the flake before (green) and after functionalization (blue), showing an average thickness increase of 4.1 nm. The average PDI coverage in all the studied flakes was 3.6 nm. The inset shows representative profiles, corresponding to the lines in the images. c) Scanning Raman microscopy (SRM) of the same flake. Left: Silicon intensity Raman map showing a decrease in the 521 cm^{-1} signal that clearly reveals the morphology of the flake. Right: Raman intensity mapping shows the exclusive self-assembly of the PDI on the antimonene flakes and not on the Si/SiO₂ substrate. d) Mean Raman spectra (excitation at 532 nm) of the flake showing the PDI bands as a consequence of the quenching of its fluorescence. The correlation between the PDI ν_{Ag} Raman intensities and the flake thicknesses is highlighted in the inset. Reproduced with permission.^[63]

Antimonene, a single layer of antimony atoms, is a promising 2D material with potential applications in a variety of technological fields, including optoelectronics and energy harvesting. Recently, the isolation of a single layer of antimonene opened the door to the possibility of realizing these predictions. In this work, recent progresses on antimonene are reviewed.

2D Materials, Antimonene, Black Phosphorus, Theoretical Calculations, 2D Materials Preparation

P. Ares, J. J. Palacios, G. Abellán, J. Gómez-Herrero*, F. Zamora*

Recent progress on antimonene: a new bidimensional material

